

# 1      **Refined InSAR method for mapping and classification of active** 2      **landslides in a high mountain region: Deqin County, southern** 3      **Tibet Plateau, China**

4      **Xiaojie Liu <sup>a, b, c</sup>, Chaoying Zhao <sup>a, d \*</sup>, Yueping Yin <sup>e \*</sup>, Roberto Tomás <sup>c</sup>, Jing Zhang <sup>a</sup>, Qin Zhang <sup>a, d</sup>,**  
5      **Yunjie Wei <sup>e</sup>, Meng Wang <sup>f</sup>, Juan M. Lopez-Sanchez <sup>g</sup>**

6      <sup>a</sup> School of Geological Engineering and Geomatics, Chang'an University, Xi'an 710054, China.

7      <sup>b</sup> School of Civil Engineering, Lanzhou University of Technology, Lanzhou 730050, China.

8      <sup>c</sup> Department of Civil Engineering, University of Alicante, Alicante 03080, Spain.

9      <sup>d</sup> Key Laboratory of Western China's Mineral Resources and Geological Engineering, Ministry of Education, Xi'an  
10      710054, China.

11      <sup>e</sup> China Institute of Geo-environment Monitoring, Beijing 10081, China.

12      <sup>f</sup> Sichuan Geological Survey, Chengdu 610081, China.

13      <sup>g</sup> Institute for Computer Research (IUII), University of Alicante, Alicante 03080, Spain.

14      \* Correspondence: [cyzhao@chd.edu.cn](mailto:cyzhao@chd.edu.cn); [yinypcgs@hotmail.com](mailto:yinypcgs@hotmail.com);

## 15      **Abstract**

16      The mapping and classification of active landslides in high mountainous regions provide crucial  
17      information about the location and types of geohazards. Additionally, this process plays a vital role in ensuring  
18      the safety of the geological environments in mountainous towns. In this study, we presented a refined InSAR  
19      approach for mapping and classifying active landslide hazards in Deqin County, Tibetan Plateau, China. The  
20      study area is characterized by a high altitude and extremely rugged terrain. Consequently, conventional InSAR  
21      methods are limited in precisely estimating landslide deformation owing to severe atmospheric delays. To this  
22      end, we first propose a block-based linear model to correct tropospheric artifacts. This model considers the  
23      spatial variability of the atmosphere and provides an opportunity to accurately estimate heterogeneous

24 atmospheric delays over high mountainous areas without any external data. Compared with the traditional  
25 global-window linear model and the GACOS approach, the new method demonstrated outstanding performance  
26 in reducing atmospheric artifacts. Second, based on the knowledge mapping of landslide types, we proposed a  
27 semi-automatic procedure to map and classify landslides using InSAR-derived displacements and auxiliary data  
28 (i.e., C-index and high-resolution optical images). Our results obtained from ascending and descending  
29 Sentinel-1 images revealed, for the first time, that there were 317 active landslides in Deqin County between  
30 May 2017 and June 2021. Among these, 10.7% were associated with slide activity, 7.9% with fall deformation,  
31 and the majority (81.4%) with flow movement. These results were cross-verified and evaluated using an a priori  
32 inventory map obtained from the visual interpretation of optical images and geological field surveys. This study  
33 demonstrates that InSAR can accurately map and classify active landslides over difficult mountainous terrains,  
34 provided the associated phase errors are effectively restrained.

35 **Keywords:** Landslides, time series InSAR, tropospheric delay correction, Tibetan Plateau, Deqin County

## 36 1 Introduction

37 Mountainous regions are home to 12% of the world's population and cover 24% of global land area (Hock  
38 et al., 2019). They are characterized by high elevations, sharp topographic gradients, and paraglacial  
39 environments; therefore, under the combined effects of tectonic activity and extreme precipitation, mountainous  
40 regions are also the origin of landslide hazards (Mani et al., 2023), including various types of movement  
41 processes (falls, slides, and flows) according to the classification system of Varnes (1978). In particular, it has  
42 been demonstrated in the scientific literature (e.g., Gariano and Guzzetti, 2016) that the magnitude and  
43 frequency of landslide occurrences have increased in high mountainous areas in recent years due to the coupling  
44 effects of population growth and climate change. Over the past ten years (2013–2023), the world's high  
45 mountainous regions have experienced several major landslide hazards that have resulted in numerous fatalities  
46 and/or serious damage to local infrastructure. For example, approximately 25000 landslides were triggered by  
47 the 2015 Mw7.8 Gorkha (Nepal) earthquake, which destroyed several villages and important infrastructure, and  
48 killed 8200 people (Roback et al., 2018); the heavy rainfall event in the European Alps in October 2020 resulted  
49 in more than 20 deaths and widespread destruction of infrastructure and settlements (Mani et al., 2023); and the  
50 2021 Chamoli (India) rock/ice avalanche event killed more than 200 people and caused severe damage to two  
51 hydropower projects (Shugar et al., 2021). Of these, the Qinghai-Tibet Plateau and its surroundings are regions

52 with the most severe high-altitude landslide hazards worldwide. For instance, a huge landslide occurred in  
53 Yigong, Tibet (China) in April 2000, and tens of thousands of people from China and India were seriously  
54 affected by this event (Yin et al., 2023); two successive landslides in eastern Tibet (China) occurred on October  
55 10 and November 3, 2018, and economic losses in several billion Chinese Yuan were caused by this event (Liu  
56 et al., 2020). Consequently, it is paramount to gain detailed knowledge of active landslides for the sustainable  
57 development of mountainous regions and the mitigation of hazard risks (Mani et al., 2023). Unfortunately, the  
58 locations and types of potential landslide hazards in most high mountainous regions of the world remain largely  
59 unknown owing to the complicated geomorphology and environmental conditions mentioned above. Under  
60 these circumstances, conventional methods (e.g., field observations) present many limitations in generating and  
61 updating inventory maps. Therefore, developing effective and robust techniques to map and classify these  
62 geohazards is necessary to increase our knowledge of where the landslides are, their types, and how they may  
63 impact communities and infrastructure.

64 Interferometric synthetic aperture radar (InSAR) provides the distinctive capability to measure Earth's  
65 surface displacements over wide areas with high measurement accuracy. Advanced time series InSAR methods  
66 have been extensively used to investigate landslide deformation in small to extremely large areas for various  
67 purposes, including the detection and monitoring of active landslides (Liu et al., 2021a; Shi et al., 2019),  
68 classification of landslide processes and styles (Crippa et al., 2021), capturing the precursory signals of slope  
69 rupture (Liu et al., 2020), inferring subsurface geometry (Handwerker et al., 2021), modeling kinematic  
70 behaviors (Xie et al., 2022), and assessing the hazard and risk (Jin et al., 2022). Beyond these achievements,  
71 there are still some challenges that limit the application of InSAR in mapping and classifying landslide hazards  
72 in high mountainous regions, such as spatiotemporal decorrelation, SAR geometrical distortions, and  
73 tropospheric delays (Albino et al., 2020). Various advanced InSAR methods (e.g., Ferretti et al., 2001;  
74 Berardino et al., 2002) have been established to overcome these challenges by exploiting multisource and  
75 multitemporal SAR observations. However, the performance of time-series InSAR methods is restricted by  
76 atmospheric artifacts in high mountainous regions (Doin et al., 2009; Liang et al., 2019).

77 Approaches proposed to correct tropospheric delays in SAR images can be broadly classified into three  
78 categories. The first category corresponds to the direct use of spatiotemporal filtering or stacking methods in  
79 the interferometric phases (Ferretti et al., 2001). The second category relies on the prediction of tropospheric  
80 signals from auxiliary information, including satellite multispectral imagery (Li et al., 2006), local or global

81 weather models (Doin et al., 2009; Yu et al., 2018), and GNSS observations (Yu et al., 2017). These approaches  
82 have achieved considerable progress in atmospheric corrections in large-scale Earth surface movement  
83 processes, such as earthquake ruptures and interseismic deformation. However, the sparse temporal or spatial  
84 resolution of auxiliary data often entails the need for interpolation in the application of small-scale landslide  
85 deformation mapping, thus introducing uncertainties into the corrected interferograms (Liang et al., 2019). The  
86 third category focuses on correcting delays using empirical phase-based models in which topography-dependent  
87 phase delays are generally calculated using a linear model over all interferograms (Doin et al., 2009; Liu et al.,  
88 2021a). Such an approach is challenging in high mountainous regions because of the spatial variability of  
89 tropospheric properties (Bekaert et al., 2015). More importantly, the effects of seasonal fluctuations in  
90 tropospheric delays should also be considered because they can easily be misinterpreted as seasonal landslide  
91 displacements resulting from changes in hydrological factors. Similarly, they may lead to erroneous judgment  
92 for active landslide detection and a spurious signal for the early warning of landslide deformation.

93 The procedure for automatically collating high-precision inventory maps of landslides over wide areas  
94 based on InSAR-derived ground deformation has become an increasingly important research topic. Most  
95 existing methods prepare an inventory map of landslides by either manual decision-making (i.e., expert  
96 interpretation, comparison, and analysis) (Dong et al., 2018) or setting deformation thresholds (Shi et al., 2019),  
97 in which the spatial deformation (e.g., annual displacement rate) is the only information exploited. Manual  
98 decision-making is a time-consuming process, and the method of setting the deformation thresholds does not  
99 ensure sufficient accuracy for landslide mapping under complex geomorphic conditions (e.g., high mountainous  
100 areas) because the InSAR-derived displacements inevitably contain noise. Thus, to accomplish automated and  
101 high-precision inventory mapping, we should make full use of InSAR measurements in both spatial  
102 (displacement rate) and temporal (displacement time series) dimensions.

103 Deqin County is located on the southern edge of the Qinghai-Tibet Plateau, China, where various landslide  
104 hazards seriously threaten the population and infrastructure. Nevertheless, the geomorphological and  
105 environmental conditions in this region are complicated, with high altitude and extremely rugged terrain. This  
106 makes the estimation of landslide displacements using InSAR challenging, and there is no systematic analysis  
107 of the locations and types of active landslides. In this study, we propose a refined InSAR method to address  
108 these challenges and map and classify active landslides over the study area. To this end, we first developed a  
109 block-based linear model to correct atmospheric artifacts in the interferograms. Second, based on the InSAR-

110 derived high-accuracy displacement maps and DEM-derived C-index maps, we automatically extracted active  
111 displacement areas (ADAs). The detected ADAs were then verified and classified using information from  
112 geological field surveys and the geologist's visual interpretation of optical images, and a final inventory map  
113 of different types of landslides in the study area was produced. The proposed method contributes to the accurate  
114 correction of heterogeneous atmospheric delays and facilitates the mapping and classification of landslides in  
115 high mountainous regions using InSAR observations. These results provide valuable guidelines for managing  
116 and preventing landslide hazards and sustainable development in Deqin County.

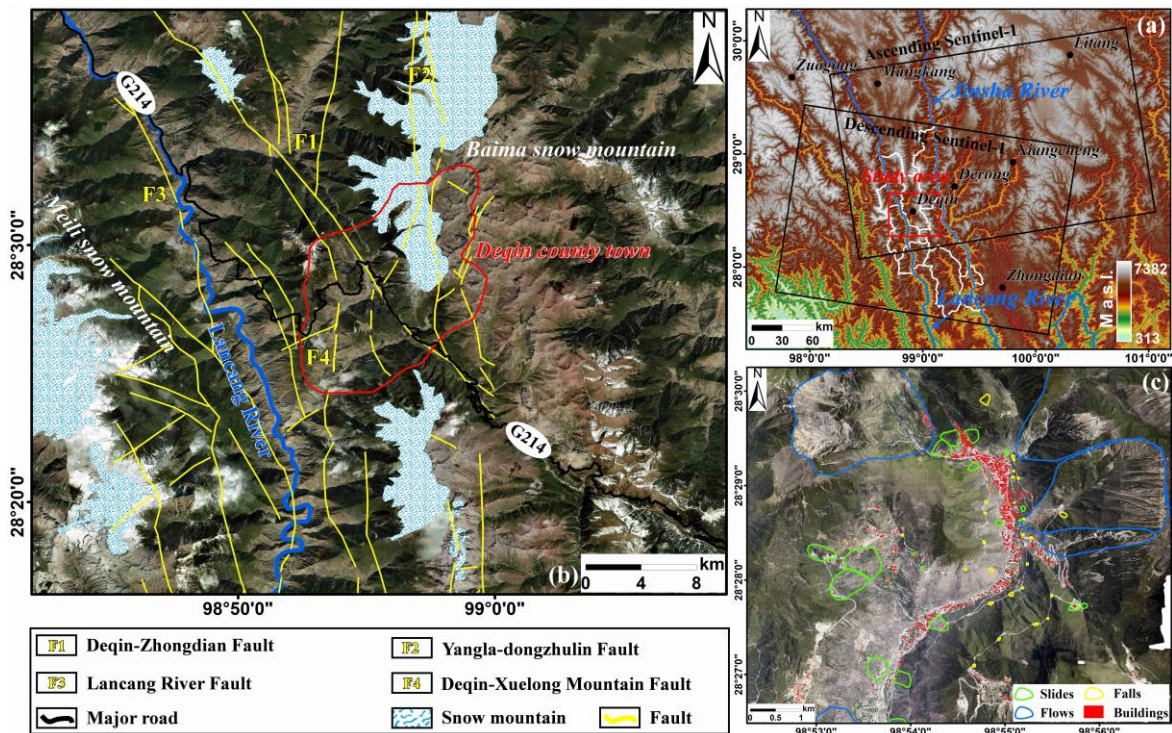
## 117 **2 Study area and datasets**

### 118 **2.1 Study area**

119 Our study area is located between 98.704 and 99.151 °E and 28.272 and 28.653 °N (red rectangle in [Fig.](#)  
120 [1\(a\)](#)) within Deqin County (white polygon in [Fig. 1\(a\)](#)), Yunnan Province, on the southern edge of the Qinghai-  
121 Tibet Plateau, China. It covers an area of approximately 1900 km<sup>2</sup> that includes the town of Deqin County, and  
122 the overview is shown in [Fig. 1\(b\)](#) using the Sentinel-2 image. The study area is a landform feature of the alpine  
123 gorge region with topographic attitudes ranging from 1924 to 6740 m a.s.l., forming a relative elevation  
124 difference of 4816 m. As a result, it is characterized by steep inner gorges, extensively distributed high-altitude  
125 glaciers, and snow mountains (e.g., the Baima and Meili snow mountains marked in [Fig. 1\(b\)](#)). The Lancang  
126 River flows through the region ([Fig. 1\(b\)](#)). Glaciers have retreated in the past few decades, and terminal  
127 moraines have been deposited, providing favorable conditions for developing debris flows.

128 The study area is underlain by a variety of stratigraphic units, including Silurian, Ordovician, Cambrian,  
129 Sinian, Proterozoic, Jurassic, Cretaceous (sandstone and slate), Devonian (limestone and siltstone),  
130 Carboniferous, Permian (bioclastic limestone, sandstone, and shale), and Triassic systems (sandstone, slate,  
131 limestone, and mudstone), in which the Permian and Triassic systems are the primary formations. More  
132 importantly, the study area is geologically situated in a zone of strong compression and is conditioned by a  
133 series of deep large faults in the north-south and north-west directions, such as the Deqin-Zhongdian fault (F1),  
134 Yangla-Dongzhulin fault (F2), Lancang River fault (F3), and Deqin-Xuelong Mountain fault (F4), as shown in  
135 [Fig. 1\(b\)](#).

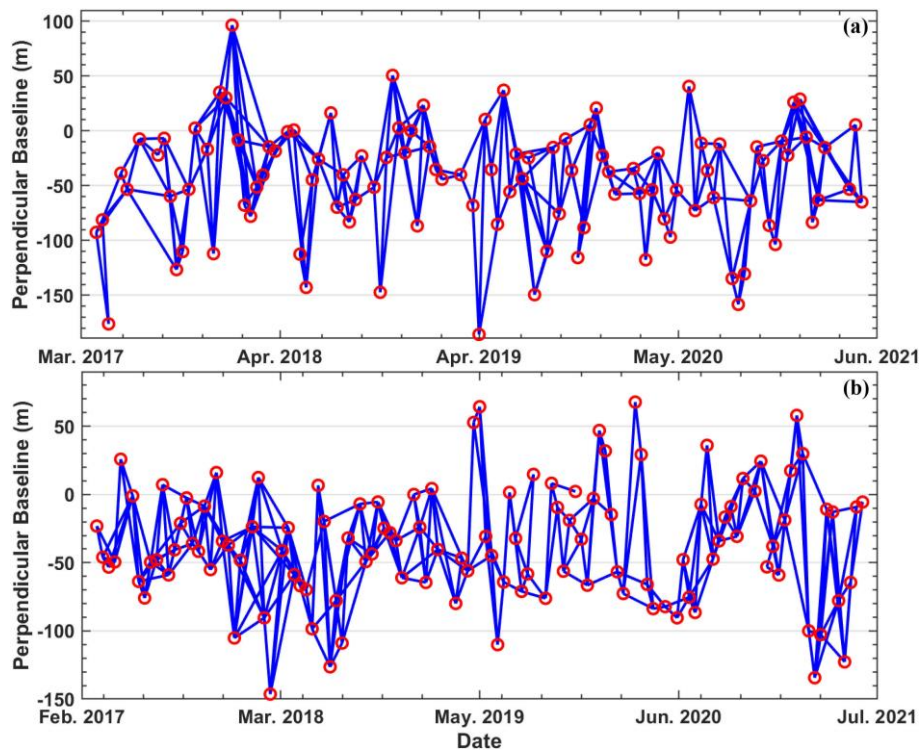
136 According to the Varnes (1978) classification system, landslide hazards, including falls, slides,  
 137 are expected to remain high in the study area because of the strong coupling of the endogenic and exogenic  
 138 geological actions mentioned above. An existing inventory map elaborated from geological field surveys and a  
 139 geologist's visual interpretation of optical images from unmanned aerial vehicle (UAV) and satellite  
 140 measurements revealed that there were 87 landslide hazards in the study area ( Fig. 1(c)), including 50 slides,  
 141 29 falls, and 8 large-scale flows. Some of the infrastructure is built on ancient landslides owing to the existing  
 142 limitations caused by the available land resources against growing populations. As shown in Fig. 1(c), people  
 143 who inhabit Deqin county town are potentially affected by the rupture of catastrophic landslide events and the  
 144 severe impacts accompanying them, including fatalities, destruction of infrastructure, and damage to settlements.  
 145 Therefore, it is crucial to map and classify landslide hazards to reduce disaster risks and sustain livelihoods in  
 146 the study area.



147  
 148 **Fig. 1.** (a) Location of the study area and spatial coverage of the Sentinel-1 SAR images, where the white  
 149 polygon indicates Deqin County; (b) overview of the study area; and (c) overview of Deqin County town (red  
 150 polygon in (b)). The UAV measurement acquired the background image in September 2020, and the polygons  
 151 with different colors are the a priori landslide hazards.

152 **2.2 SAR datasets**

153 In this study, 223 C-band Sentinel-1 SAR images were used to retrieve the displacement of the study area  
154 from March 2017 to June 2021, among which 106 images were acquired in the ascending orbit from April 11,  
155 2017, to May 8, 2021, and 117 images were acquired in the descending orbit from March 25, 2017, to June 8,  
156 2021. The spatial coverage of the SAR images is shown in Fig. 1(a). Using a combination of ascending and  
157 descending images, we aimed to a) weaken the effect of SAR geometrical distortions and b) cross-validate the  
158 estimated displacements and mapped landslides. All possible interferometric pairs were generated using the  
159 strategy of small baseline subsets (SBAS) (Berardino et al., 2002), with a maximum spatial baseline of 150 m  
160 and a maximum temporal baseline of 100 days. The interferograms were multi-looked using factors of 4 in the  
161 range and 1 in the azimuth to reduce noise, which has the ability to map slope movements as small as 100 m in  
162 each dimension. Finally, we selected 565 high-quality interferometric pairs to estimate the displacements by  
163 dropping noisy unwrapped interferograms to retrieve useful signals, among which 265 interferograms were  
164 produced from the ascending track and 300 interferograms from the descending track. Figure 2 shows the spatial  
165 and temporal baseline plots of the interferograms used in the displacement inversion.



166

167 **Fig. 2.** Spatial and temporal baseline plots of the used interferograms for ascending (a) and descending (b)  
168 Sentinel-1 images.

## 169 2.3 Auxiliary datasets

170 A set of multitemporal optical images covering the entire study area was acquired from satellite and UAV  
171 measurements to verify the landslides identified from the InSAR-derived displacements and assist in the  
172 classification of detected landslides. Satellite optical images were downloaded from the National Platform for  
173 Common Geospatial Information Services (<https://www.tianditu.gov.cn/>), with a spatial resolution of 0.6 m.  
174 We captured high-resolution (~ 0.1 m) images of the study area on September 18, 2020, using a Pegasus fixed-  
175 wing UAV manufactured by FEIMA Robotics, including a digital orthophoto map (DOM) (Fig. 1(c)), a high-  
176 resolution digital surface model (DSM), and a 3D model of the Earth's surface (Fig. S1). In addition, the 1-arc-  
177 second (30 m) DEM generated by NASA's Shuttle Radar Topography Mission (SRTM) was collected to remove  
178 the topographic phase from the interferograms and calculate the C-index maps.

## 179 3 Methodology

180 The study area is located in a high mountainous region with extremely rugged terrain; therefore,  
181 topography-correlated tropospheric delays introduce considerable measurement errors into individual  
182 interferograms. These errors hamper high-accuracy estimation of landslide deformation using the InSAR  
183 method. Abundant vegetation and ice-snow cover, which are common in high mountainous regions, are  
184 particularly problematic and result in increased noise, making InSAR detection and mapping of active landslides  
185 more difficult. Here, we developed a refined InSAR method for the semi-automatic detection and classification  
186 of active landslides in high mountainous regions. The overall technical scheme of the methodology is illustrated  
187 in Fig. 3. First, our approach generates high-accuracy ground displacement maps for the study area, including  
188 the displacement rate and time series, by performing a refined InSAR processing procedure. In this procedure,  
189 a block-based linear model was proposed to correct InSAR atmospheric artifacts over the study area. Then,  
190 InSAR-derived high-accuracy ground displacement maps and DEM-derived C-index maps were selected as  
191 input datasets, and a semi-automatic approach was developed to map and classify different types of active  
192 landslides and produce the final inventory map. The detailed procedure of the adopted methodology is described  
193 below.

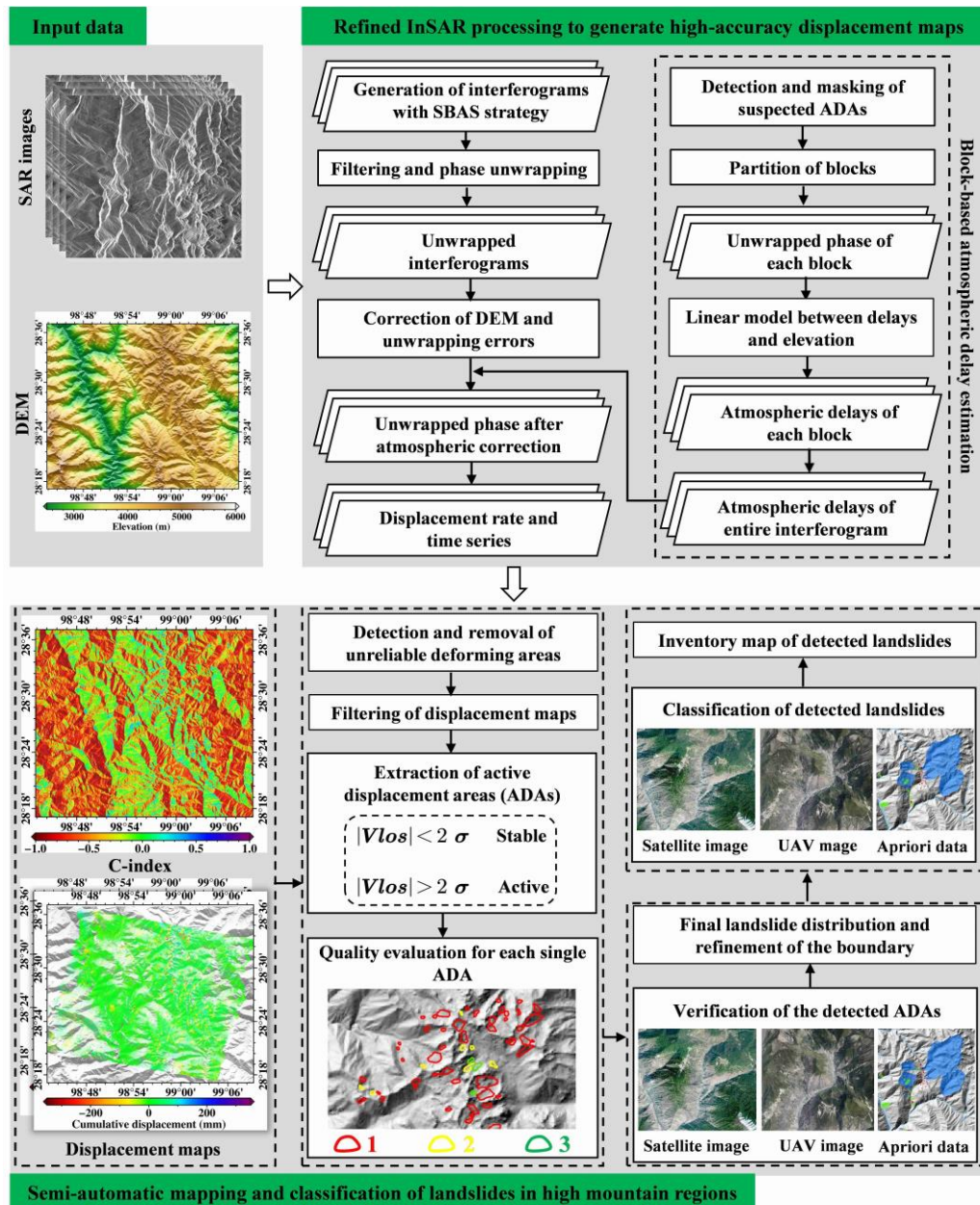
### 194 3.1 Refined InSAR processing



195 The starting point of this approach is to form all possible interferometric pairs by thresholding the spatial  
196 and temporal baselines, as outlined in [Section 3.2](#). We used the commercial GAMMA software ([Wegmuller](#)  
197 [and Werner, 1997](#)) to co-register the Sentinel-1 images and generate multiple primary multi-looked differential  
198 interferograms. The topographic and flat-Earth phases were removed using the SRTM DEM. The  
199 interferometric phase was filtered using the Goldstein filter ([Goldstein and Werner, 1998](#)) to reduce the effects  
200 of noise, and then the phase unwrapping operation was performed with the minimum cost flow (MCF) algorithm  
201 ([Costantini, 1998](#)). After the basic InSAR processing mentioned above, the unwrapped phase  $\varphi$  of each pixel  
202 can be mathematically expressed as follows:

$$203 \quad \varphi = \varphi_{def} + \varphi_{orbit} + \varphi_{tropo} + \varphi_{scatter} + \varphi_{noise} + \varphi_{error} \quad (1)$$

204 where  $\varphi_{def}$  indicates the component for the deformation phase;  $\varphi_{orbit}$  is the phase ramps resulting from  
205 orbital inaccuracy, which can be estimated by fitting second-order polynomials and is usually neglected for  
206 Sentinel-1 images with accuracy orbits;  $\varphi_{scatter}$  represents the scattering phase caused by volume decorrelation,  
207 Doppler centroid decorrelation, and spatiotemporal decorrelation;  $\varphi_{noise}$  describes the random noise resulting  
208 from co-registration error and thermal noise;  $\varphi_{error}$  is the phase errors induced by inaccurate DEM and  
209 unwrapping errors, the details for correcting such a component can be found in [Liu et al. \(2021a\)](#); and  $\varphi_{tropo}$   
210 indicates the tropospheric delays induced by changes in atmospheric state between two SAR images, which is  
211 the main source of errors and should be carefully corrected prior to deformation computation.



212

213 **Fig. 3.** Technical scheme of refined InSAR method for mapping and classifying active landslides in high  
 214 mountain regions where ADAs indicate active displacement areas.

215 The phase-based method (e.g., linear relationship between phase delay and elevation (Doin et al., 2009))  
 216 and auxiliary data, such as GACOS products (Yu et al., 2018), are typically used to correct atmospheric delays  
 217 over the entire interferogram. Three challenging factors should be considered in the detection of small-scale  
 218 landslides in high mountainous terrains with large elevation variations. First, the relationship between stratified  
 219 delay and elevation cannot be simply considered linear because of spatial and seasonal variations in tropospheric

220 properties (Doin et al., 2009). Second, the degree of success in removing atmospheric delays with auxiliary data  
221 is sensitive to the time gap between SAR and data acquisitions (Bekaert et al., 2015). The last was to avoid the  
222 removal of landslide deformation signals when the deformation was correlated with elevation. Consequently, a  
223 block-based linear model (hereinafter referred to as the BLM method) was developed in this study to deal with  
224 the tropospheric delay in high mountainous regions. The refined InSAR processing procedure was achieved by  
225 adding a BLM atmospheric correction to the ordinary SBAS-InSAR algorithm (Berardino et al., 2002), as  
226 follows:

227 (1) The ordinary SBAS-InSAR approach was exploited to generate all possible differential interferograms  
228 and obtain their unwrapped phases with corrections for orbital, DEM, and unwrapped errors.

229 (2) The tropospheric delays were initially estimated using GACOS atmospheric products and a traditional  
230 linear phase-based model (Eq. (2)) over the entire interferogram (hereafter referred to as the GLM method) and  
231 then removed from the unwrapped interferograms generated in Step (1).

232 (3) The preliminary displacement rate and time series are estimated from the unwrapped interferograms  
233 generated in Step (2) using the SBAS-InSAR algorithm. The derived displacement maps determined the  
234 suspected active displacement areas (ADAs).

235 (4) The suspected ADAs are masked from the interferograms generated in Step (1) to produce a new stack  
236 of displacement-free unwrapped interferograms. It aims to avoid 1) biased estimation of atmospheric delays  
237 due to ground displacements and 2) removal of the displacement signals of interest.

238 (5) The tropospheric delays were re-estimated by applying the BLM method to the displacement-free  
239 unwrapped interferograms generated in Step (4). The final unwrapped interferograms with atmospheric  
240 corrections were then obtained by subtracting the estimated atmospheric delays from the interferograms  
241 generated in Step (1). The rationale for the BLM atmospheric correction method is described in Section 3.2.

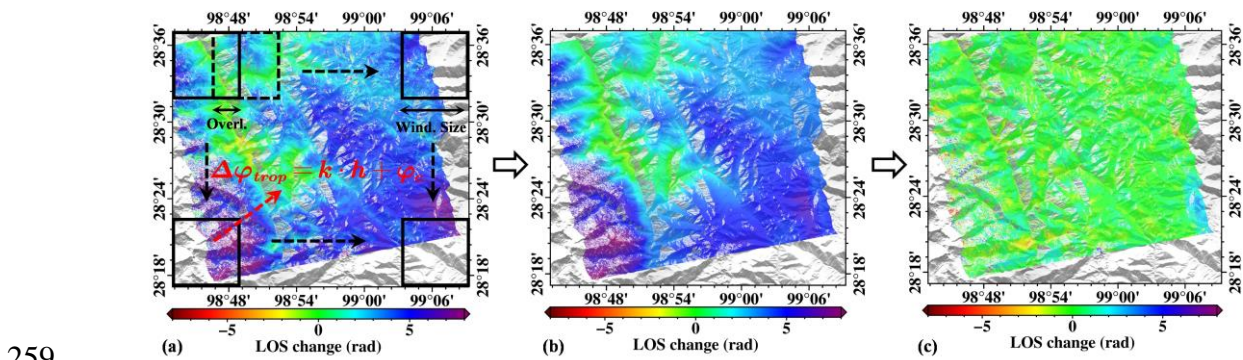
242 (6) The final displacement rate and time series are re-estimated using the high-quality unwrapped  
243 interferograms generated in Step (5).

### 244 3.2 Block-based linear model for atmospheric correction

245 The vertically stratified component of tropospheric delays ( $\Delta\phi_{trop}$ ) in interferograms can be empirically  
246 calculated using the best-fitting linear relationship between the elevation and the phase delay as follows (Doin  
247 et al., 2009):

248 
$$\Delta\varphi_{trop} = k \cdot h + \varphi_c \quad (2)$$

249 where  $k$  and  $h$  are the delay-elevation ratio and elevation, respectively, and  $\varphi_c$  denotes the phase at zero  
 250 elevation. The elevation  $h$  was obtained using an external DEM. As mentioned above, it is difficult to  
 251 accurately estimate the atmospheric delay with a unified delay-elevation ratio for an entire interferogram in  
 252 high mountainous regions. Thus, we propose a block-based linear model for estimating and correcting the  
 253 vertically stratified phase delay, the rationale for which is presented in Fig. 4. Considering the properties of the  
 254 stratified phase delay, the new method is based on a linear relationship (Eq. (2)) between the elevation and  
 255 phase delay. The largest difference from the ordinary phase-based approach is that, in our method, the  
 256 displacement-free unwrapped interferograms are first partitioned into several blocks (Fig. 4(a)). The  
 257 atmospheric delay was estimated for each block using Eq. (2). Finally, the estimated delays of all blocks were  
 258 mosaiced to produce tropospheric artifacts for the entire interferogram (Fig. 4(b)).



260 **Fig. 4.** Rationale of the block-based linear model for atmospheric correction. Overl. represents the overlapping  
 261 region between two adjacent blocks and Wind. Size is the size of each block.

262 **Step 1: Partition of blocks and generation of atmospheric delays.** The entire scene of the interferogram  
 263 is partitioned into multiple blocks (Fig. 4(a)), and each block has a size of  $m \times m$  pixels (i.e., block size) in the  
 264 range and azimuth directions. Additionally, there is an overlapping region of  $p$  columns and  $q$  rows in the  
 265 range and azimuth directions between two adjacent blocks. The block size (i.e., Wind. Size in Fig. 4(a)) is  
 266 determined based on the magnitude of the heterogeneous atmospheric delay and the scale of the maximum  
 267 deforming area. The evidence from Barnhart and Lohman (2013) demonstrated that the topography-correlated  
 268 atmospheric delays are not spatially stationary in individual interferograms, even over small-spatial extents (<  
 269 10 km). Therefore, the block size should be larger than the maximum deforming area size and smaller than 10

270  $\times 10$  km in mountain areas. In this study, we set the block size as  $300 \times 300$  pixels in the azimuth and range  
271 directions after a series of tests, and the overlapping region between two adjacent blocks is equal to 25% of the  
272 block size. Then, for each block, the atmospheric delay is estimated with Eq. (2) based on the selected  $M$  pixels  
273 (i.e., ), this can be mathematically written as follows:

$$274 \quad AX + \delta = L \quad (3)$$

275 where  $A$  is the coefficient matrix,  $L = [\varphi_{tropo}^1 \ \varphi_{tropo}^2 \ \cdots \ \varphi_{tropo}^M]$  denotes the unwrapped phase in each block, and  
276  $X$  is an unknown parameter, that is, the coefficients  $k$  and  $\varphi_c$  in Eq. (2), and  $\delta$  indicates a systematic  
277 error. The least-squares criterion or linear regression is typically used to estimate the unknown parameter  $X$   
278 as follows:

$$279 \quad \hat{X} = (A^T P A)^{-1} A^T P L \quad (4)$$

280 where  $P$  is the weight matrix. It is worth noting that outliers in the interferograms caused by phase noise and  
281 unwrapping errors can introduce biases into the estimated atmospheric delays. Thus, we adopted the iterative  
282 weighted least squares (IWLS) algorithm (Huber, 1964) to estimate the unknown parameter  $X$  and limit the  
283 influence of gross errors.

284 **Step 2: Mosaicking the estimated atmospheric delays of all blocks.** After estimating the tropospheric  
285 delays of each block, the atmospheric artifacts of the entire scene of the interferogram were produced by  
286 mosaicking the delays of all blocks (Fig. 4(b)). Because the tropospheric delay of each block was calculated  
287 independently, there was inevitably a phase shift between two adjacent blocks. To address this issue, the phase  
288 difference and average phase value in the overlapping region were calculated to compensate for this shift.  
289 Moreover, considering the strong spatial correlation of the stratified phase delay, phase shifts in the mosaicked  
290 atmospheric products were eliminated using an average filtering procedure.

291 **Step 3: Correction of the tropospheric delays.** Finally, the estimated atmospheric delays were subtracted  
292 from each unwrapped interferogram to generate a corrected ground displacement map (Fig. 4(c)).

### 293 3.3 Semi-automatic mapping of active landslides

294 Based on the high-accuracy displacement maps derived from the refined InSAR method, coupled with C-  
295 index maps derived from the external DEM, an a priori inventory map of landslides (Fig. 1(c)), and multi-

296 temporal optical remote sensing images, we present a semi-automatic approach for detecting and mapping  
297 active landslides in high mountainous regions, as shown in Fig. 3. The proposed method is composed of two  
298 sequential modules: (i) extraction of suspected active displacement areas (ADAs) and (ii) generation of the final  
299 landslide distribution and refinement of their active boundaries.

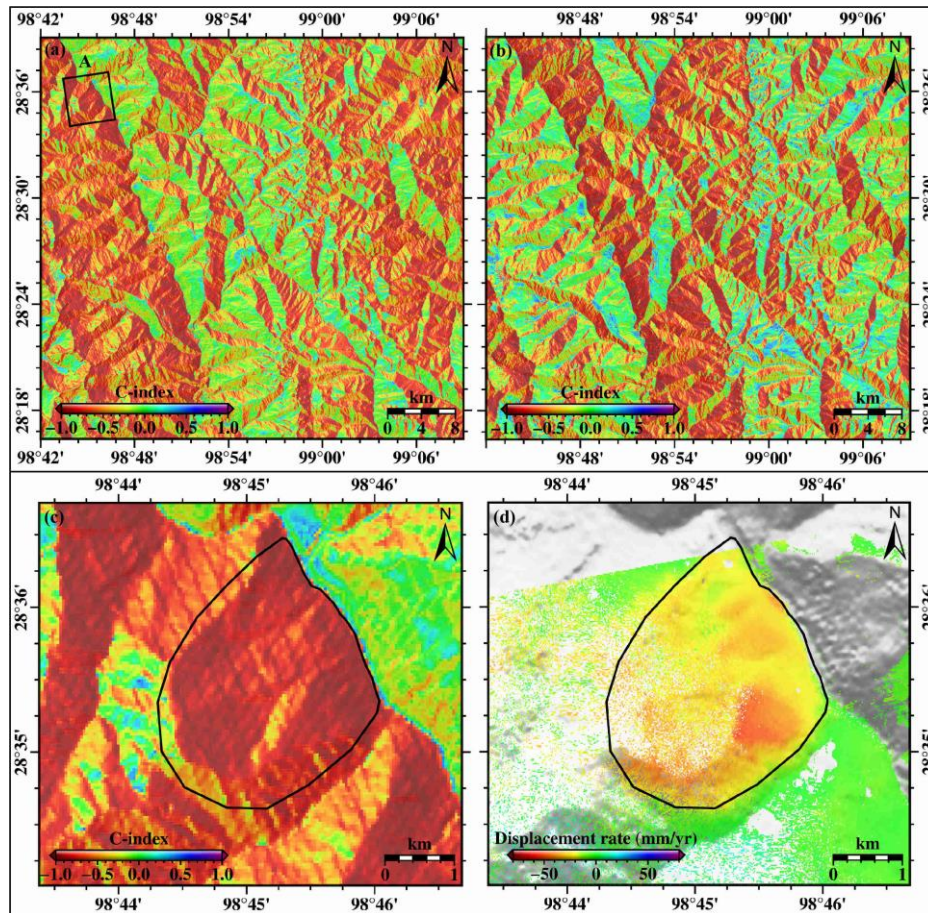
300 **(i) Extraction of suspected active displacement areas (ADAs).** This module aims to generate highly  
301 reliable suspected active displacement areas (ADAs) with high reliability. Consequently, we first detected and  
302 removed unreliable deforming areas caused by SAR geometrical distortions, phase-unwrapping errors, and  
303 residual atmospheric artifacts, which were achieved using C-index maps. The C-index was calculated using an  
304 external DEM based on the imaging parameters of the SAR images and is defined in Eq. (5).

$$305 \quad C\text{-index} = -\sin \theta \cos \alpha \sin \delta \cos \beta + \sin \theta \sin \alpha \cos \delta \cos \beta - \cos \theta \sin \beta \quad (5)$$

306 where  $\theta$  and  $\alpha$  are the incidence angle and flight direction of the SAR satellite, respectively, and  $\delta$   
307 and  $\beta$  are the azimuth and slope angle of the slope, respectively. Figs. 5(a) and (b) show the C-index map of  
308 the study area for the ascending and descending Sentinel-1 images, calculated using Eq. (5), respectively. The  
309 value of the C-index is in the range of -1 to 1. InSAR-derived line-of-sight (LOS) displacements are typically  
310 defined as positive (negative) values when a landslide moves towards (away from) a SAR sensor. Therefore, a  
311 positive value of the C-index corresponds to a positive LOS displacement derived from InSAR, that is, the  
312 landslide displacement towards the SAR satellite. In contrast, a negative value of the C-index indicates a  
313 negative LOS displacement; that is, the landslide displacement is away from the satellite. Pixels were discarded  
314 if the displacement features did not follow the aforementioned rationale. The active displacement area in Region  
315 A, marked in Fig. 5(a), was selected as an example to explain how to use the C-index to remove unreliable  
316 deformation areas caused by errors. Fig. 5(c) shows the C-index map of region A for the ascending Sentinel-1  
317 image, and Fig. 5(d) shows the displacement rate of region A calculated from the ascending Sentinel-1 images.  
318 We can observe that the value of the C-index is negative, and the displacement rate is negative. The  
319 displacement direction derived from the C-index is consistent with that derived from the InSAR displacement  
320 rate. Therefore, Region A was considered a reliable active displacement area and was retained for further  
321 processing. The displacement maps were then filtered using window-based spatial filtering (Barra et al., 2017;  
322 Tomás et al., 2019) to generate spatially consistent displacement results, and the isolated pixels and pixels with  
323 strong inconsistencies with respect to their neighbors were further removed. Finally, suspected ADAs were

324 extracted using the filtered displacement rates and their standard deviations ( $\sigma$ ). A pixel is defined as a  
325 suspected active target in the case of  $|V_{los}| > 2\sigma$ , otherwise, it is considered a stable target. Suspected ADAs  
326 are automatically delineated by grouping the detected active pixels, for which pixels are clustered in the same  
327 ADA if the distance between them is smaller than the defined clustering radius (e.g., twice the spatial resolution  
328 of the SAR image) (Tomás et al., 2019). Only the displacement rate is involved in determining the ADAs in  
329 this step. Therefore, some of the detected ADAs may be affected by noise. Therefore, we further evaluated the  
330 quality of each detected ADA using a displacement time series. A quality index (QI) associated with four classes,  
331 that is, Class 1, Class 2, Class 3, and Class 4, was introduced to evaluate the degree of reliability of the detected  
332 ADAs. The rationale for calculating QI and its interpretation can be found in Barra et al. (2017) and Tomás et  
333 al. (2019).

334 **(ii) Generation of the final landslide distribution and refinement of their active boundaries.** ADAs  
335 with the worst quality (i.e., Class 4) were discarded directly, and those with Classes 2 and 3 were further verified  
336 and screened using high-resolution satellite and UAV optical images (Fig. S1), based on the deformation signs  
337 of the slopes (i.e., sliding masses, cracks, and scarps) and a prior inventory map of the landslides (Fig. 1(c)).  
338 Misjudged ADAs were eliminated; thus, a final map of the distribution of active landslides was produced. Next,  
339 the boundary of each detected landslide was manually refined according to the geomorphological features  
340 derived from high-resolution optical images.



341

342 **Fig. 5.** (a) and (b) are the C-index maps of the study area for the ascending and descending Sentinel-1 images,  
343 respectively; (c) is the C-index map of region A (marked in (a)) for the ascending Sentinel-1 image; and (d) is  
344 the displacement rate of region A calculated using the ascending Sentinel-1 images.

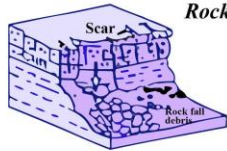
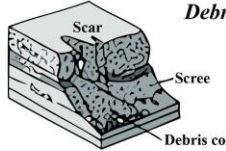
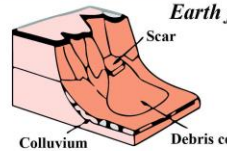
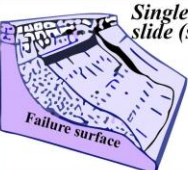
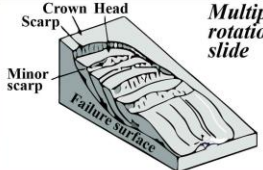
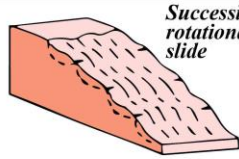
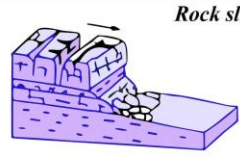
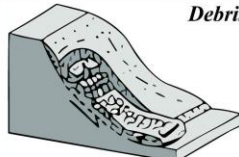
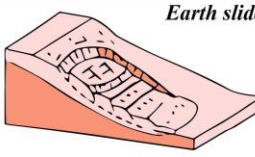
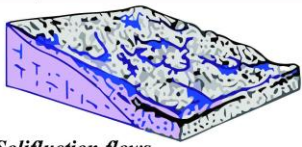
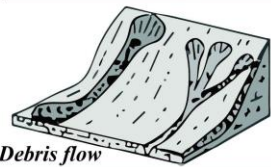
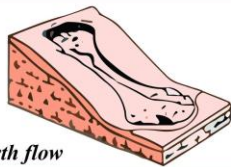
### 345 3.4 Classification of detected active landslides

346 The detected landslides were classified based on their geomorphological characteristics and divided into  
347 categories of falls, slides, and flows according to the Varnes (1978) classification system, thus producing an  
348 inventory map of the different types of landslides. The classification was achieved through an a priori inventory  
349 map of landslides (Fig. 1(a)) and the geomorphological analysis of high-resolution UAV DOM and 3D model  
350 (Figs. 1(c) and S1) based on the knowledge mapping of landslide types summarized by Varnes (1978), as shown  
351 in Fig. 6. It is worth noting that landslides are classified based on the movement type rather than the geological  
352 material because it is difficult to obtain the material for each slope using only remote sensing techniques. The  
353 term “falls” refers to masses of materials such as rock, debris, and earth that are detached from steep slopes and  
354 cliffs. The term “slides” refers to mass movements, where a failure surface separates the slide material from



355 more stable underlying material, which includes two major types of translational slides and rotational slides.

356 The term “flows” comprises three basic categories: Solifluction flows, Debris flow, and Earth flow.

Material Movement type		Rock	Debris	Earth
Falls		 <i>Rock fall</i>	 <i>Debris fall</i>	 <i>Earth fall</i>
	Rotational	 <i>Single rotational slide (slump)</i>	 <i>Multiple rotational slide</i>	 <i>Successive rotational slide</i>
Slides	Translational	 <i>Rock slide</i>	 <i>Debris slide</i>	 <i>Earth slide</i>
	Flows	 <i>Solifluction flows</i>	 <i>Debris flow</i>	 <i>Earth flow</i>

357

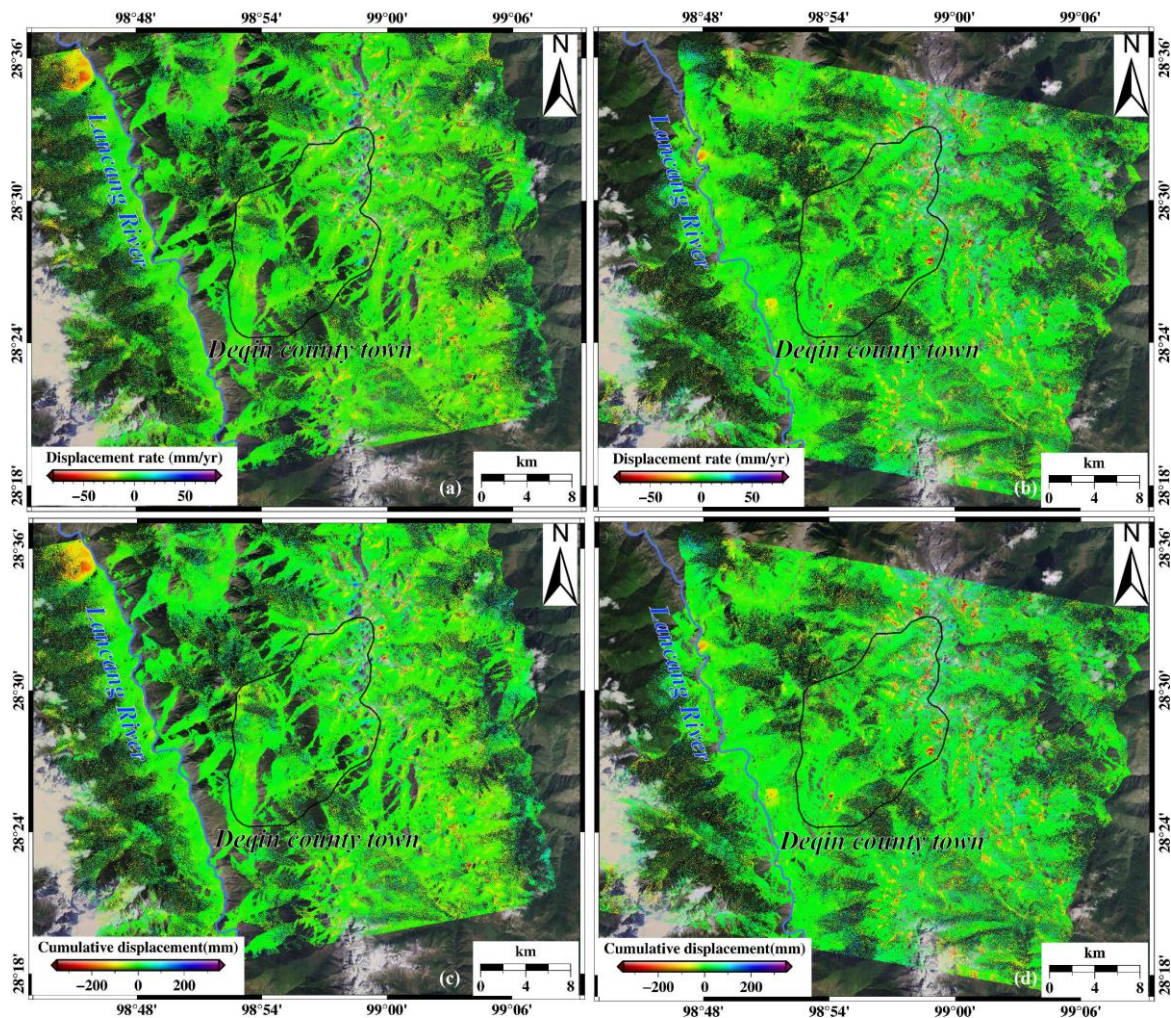
358 **Fig. 6.** Knowledge mapping of landslide types, modified from Varnes (1978).

## 359 4. Results and analyses

### 360 4.1 Displacement maps derived from refined InSAR method

361 The displacement rates and time series in the study area were calculated using ascending and descending  
 362 Sentinel-1 images based on the proposed refined InSAR processing method. **Figures 7(a)** and **(c)** show the  
 363 annual displacement rate and cumulative displacement derived from the ascending track between April 2017  
 364 and May 2021, respectively. **Figures 7(b)** and **(d)** show the annual displacement rate and cumulative  
 365 displacement derived from the descending track between March 2017 and June 2021, respectively. As shown  
 366 in **Fig. 7**, the active displacement areas (ADAs) and deformation patterns estimated from the ascending and  
 367 descending images present significant differences in some regions, such as those along the Lancang River. A  
 368 large deformation area on the right bank of the Lancang River was successfully observed in the ascending  
 369 images; however, it was not observed in the descending images. In contrast, two relatively small deforming  
 370 areas on the left bank of the Lancang River were successfully observed in the descending images but were

371 missed in the ascending images. This is caused by the different radar imaging geometries of the ascending and  
372 descending Sentinel-1 images. The ascending images are severely affected by the geometrical distortion of the  
373 layover on the left bank of the Lancang River, whereas the descending images are severely affected by the  
374 layover on the right bank. The displacement maps in Fig. 7 suggest that the ascending and descending images  
375 complement the mapping of active landslides in mountainous regions.



376

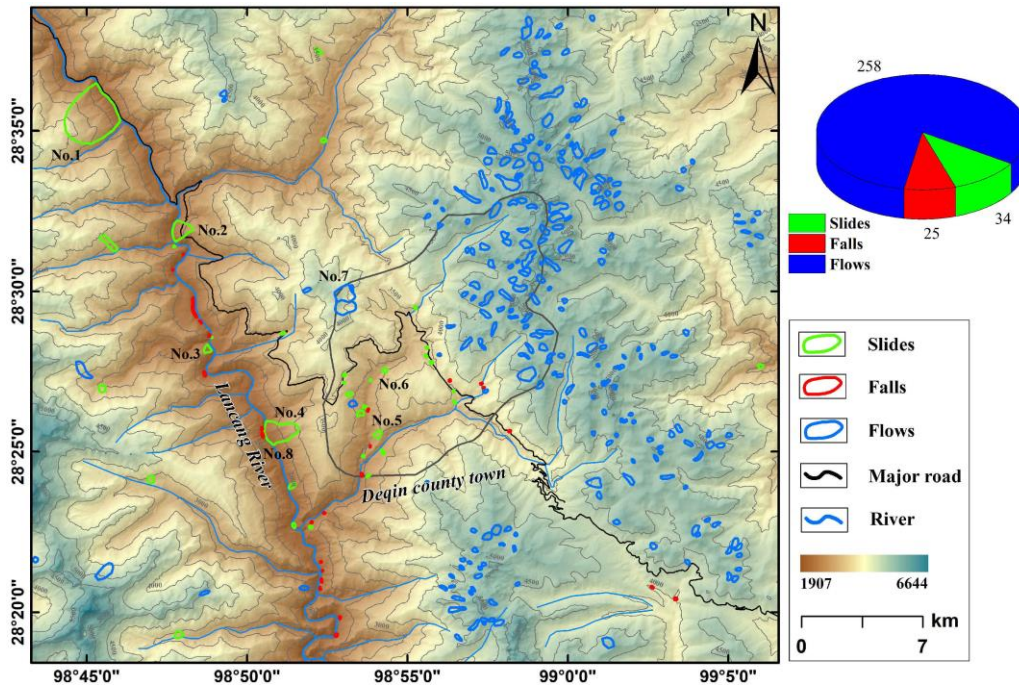
377 **Fig. 7.** (a) and (c) show the annual displacement rate and cumulative displacement of the study area derived  
378 from the ascending Sentinel-1 images from April 2017 to May 2021, respectively, and (b) and (d) show the  
379 annual displacement rate and cumulative displacement derived from the descending Sentinel-1 images from  
380 March 2017 to June 2021, respectively.

381 Displacement signals were observed in the study area for both the ascending and descending results. The  
382 maximum annual displacement rate exceeded 130 mm/year, and the largest cumulative displacement exceeded

383 600 mm. Evidence from optical images suggests that these displacements were caused by multiple landslide  
384 hazards, including slides, falls, and flows. The active displacement areas (ADAs) caused by slides and falls  
385 were primarily distributed in the town of Deqin County (black polygon marked in Fig. 7) and along the Lancang  
386 River (blue line in Fig. 7) at relatively low altitudes. In contrast, the ADAs caused by flows were concentrated  
387 in areas with a relatively high altitude, some of which were close to the town of Deqin. The InSAR  
388 displacements suggest that the detected slides and falls belong to the category of “very slow” and “slow” based  
389 on the landslide velocity classification system defined by [Hung et al. \(2013\)](#), with all displacement rates smaller  
390 than 90 mm/year. As expected, the displacement rates of the detected flows are considerably greater than those  
391 of the detected slides and falls, exhibiting a maximum annual velocity of -134 mm/year.

#### 392 **4.2 Inventory map of the detected active landslides**

393 Based on the methodology described in [Sections 3.3](#) and [3.4](#), we generated an inventory map of active  
394 landslides in the study area using displacement maps obtained from the ascending and descending Sentinel-1  
395 datasets, as shown in [Fig. 8](#). A total of 317 active landslides were detected and mapped, covering an area of  
396 approximately 1417 km<sup>2</sup>, where approximately 10.7% (i.e., 34) were related to slide activities, 7.9% (i.e., 25)  
397 were fall displacements, and 81.4% (i.e., 258) were the movements of flows. The number of flows was far  
398 greater than that of slides and falls, indicating that high-altitude flows dominated the geohazards in the study  
399 area. As shown in [Fig. 8](#), the distribution of these landslides is relatively regular across the study area. Slides  
400 and falls primarily develop along the Lancang River and roads, where the elevation is less than 3600 m a.s.l.  
401 This suggests that river erosion and human engineering activities significantly influence the formation and  
402 development of slides and fall hazards. Flow hazards were distributed in areas with altitudes higher than 4000  
403 m a.s.l. These areas belong to the high mountains of alpine-temperature and humid climate zones, which are  
404 characterized by glarosion, snowmelt runoff erosion, and freeze-thaw action, thus providing favorable  
405 conditions for the development of flow hazards.



406

407 **Fig. 8.** Inventory map of active landslides detected by ascending and descending Sentinel-1 images. Note that  
408 the detected landslides were classified according to the classification system of Varnes (1978).

409 Among these detected landslides, seven large-scale landslide hazards, composed of six slides and one flow,  
410 showed an extremely high risk of destroying buildings and infrastructure and blocking the Lancang River in the  
411 case of their runout. The spatial locations of these landslides are shown in Fig. 8 (Nos.1–7), and their main  
412 features are summarized in Table 1. Additionally, Fig. S2 shows the spatial location and 3D views of the four  
413 blocked-river landslides. The largest slopes are the Yagong landslide (labeled No. 1 in Fig. 8) and Zhixi River  
414 landslide (labeled No. 7 in Fig. 8), with areas of approximately 6.40 and 5.35 km<sup>2</sup>, respectively. According to  
415 the on-site geological survey, the Zhixi River landslide (see Section 4.4.2 for details) exhibited high mobility  
416 and strong destructive power, thus having the potential to hit Deqin County town and cause the loss of lives and  
417 property. A similar lesson was learned from the Zhouqu debris flow that occurred on August 7, 2010 (Zhang et  
418 al., 2018). The smallest active landslide was the Meili primary school landslide (labeled No. 6 in Fig. 8; see  
419 Section 4.4.1 for details), with an area of 0.05 km<sup>2</sup>. Although the landslide covered a relatively small area, it  
420 posed a high risk because of the destructive potential of the Meili Primary School and its adjacent buildings in  
421 case of rupture. Consequently, continuous displacement monitoring using InSAR and in situ facilities is  
422 suggested for this landslide in the following time. As shown in Fig. S2, despite some landslides (e.g., Niuba  
423 and Jianwangtong) cannot directly lead to damage; however, they can indirectly result in significant losses by

424 the geohazard chain of “landslide-landslide dam-flood outburst.” The best lessons can be learned from the Baige  
425 landslide, which occurred on October 11 and November 3, 2018 (Liu et al., 2020).

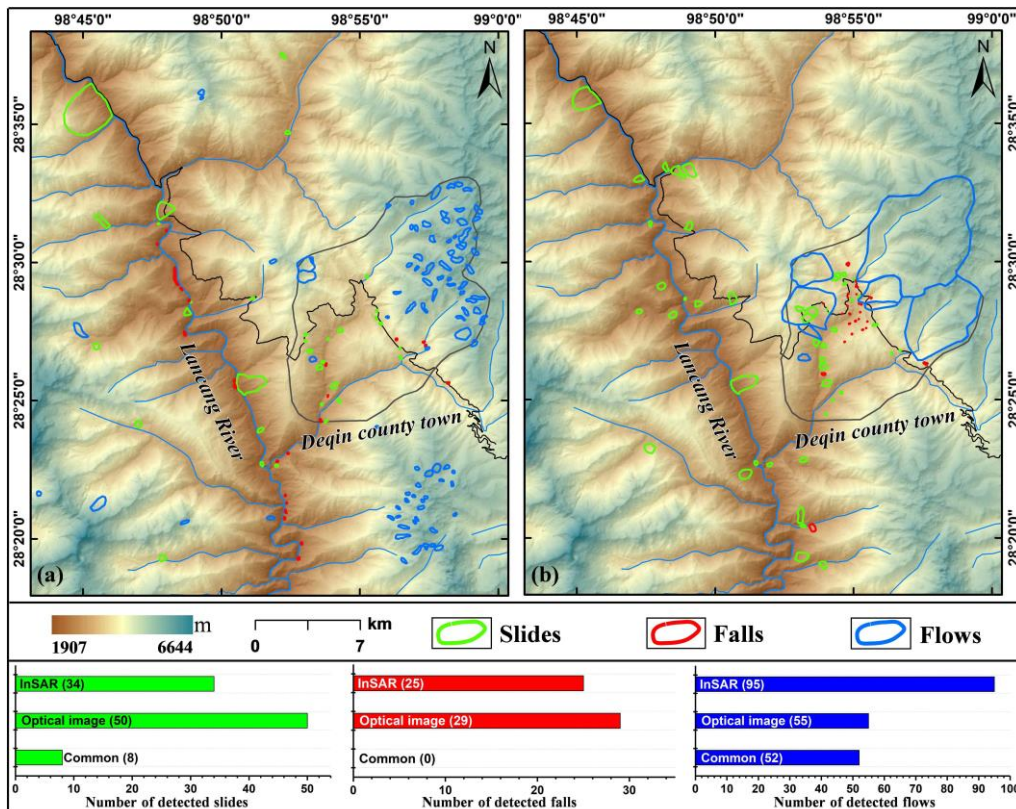
426 **Table 1.** Summary of information on seven large-scale, high-risk landslides.

No.1	Name	Type	Longitude (°)	Latitude (°)	Length (km)	Width (km)	Area (km <sup>2</sup> )
1	Yagong	Slide	98.752533	28.591168	3.29	2.58	6.40
2	Niuba	Slide	98.798454	28.531589	1.23	0.93	0.76
3	Bucun	Slide	98.812678	28.469544	0.50	0.35	0.12
4	Jianwangtong	Slide	98.851301	28.427354	0.95	0.48	0.38
5	Gongshui	Slide	98.901253	28.425466	0.46	0.56	0.12
6	Meili primary school	Slide	98.905180	28.458876	0.26	0.22	0.05
7	Zhixi River	Flow	98.882241	28.496845	2.95	1.72	5.35

### 427 4.3 Comparison of the a priori landslide inventory map and that mapped by InSAR

428 InSAR and optical remote sensing (including satellite and UAV measurements) are mature techniques that  
429 have been extensively used to prepare inventory maps of landslide hazards. On the one hand, the two techniques  
430 are complementary in mapping landslide hazards; on the other hand, the mapped results can be cross-validated.  
431 Therefore, we qualitatively compared the landslides mapped by InSAR-derived displacements and those  
432 delineated by the geologist’s visual interpretation of multitemporal satellite and UAV optical images in terms  
433 of regional-scale spatial distribution, as shown in Fig. 9. There were differences in the number and spatial  
434 distribution of landslides identified by the two methods. InSAR detected a total of 34 slide hazards, and 50 were  
435 identified by optical images, of which only eight slides were simultaneously detected by these two methods.  
436 The fall classification detected by InSAR was 25, and that detected by optical images was 29. There was no  
437 overlap between the results detected by these two methods. However, a large overlap of 52 flow cases was  
438 observed between the InSAR and the optical images. Such differences can be explained by the following aspects:  
439 (1) the effects of SAR geometrical distortions, including layover and shadowing. Geometric distortions can lead  
440 to blind areas in SAR observations, thereby generating omissions in landslide detection. Although we weakened  
441 this influence by combining the ascending and descending images, some areas are still difficult to observe in

442 any of the ascending and descending images. (2) Complex observational environments decrease the capabilities  
 443 of InSAR displacement measurements. The study area is characterized by dense vegetation and a permanent  
 444 cover of ice and snow, which can result in the decorrelation of SAR images. Consequently, vegetated and snowy  
 445 slopes have a high probability of omission from InSAR observations. (3) InSAR is sensitive to downslope  
 446 deformation. SAR satellites measure the LOS projection of a three-dimensional slope movement. This implies  
 447 that landslides were omitted when their displacements were perpendicular to the LOS direction. (4) The  
 448 constraint of spatial resolution constraints of Sentinel-1 images. The spatial resolution of the multi-looked  
 449 Sentinel-1 products is approximately 15 m in the ground direction, making it challenging to map landslides  
 450 smaller than 100 m. By contrast, the optical images obtained from the UAV had a spatial resolution of 0.1 m.  
 451 This provides an opportunity to detect small-scale slopes, even those smaller than 100 m. (5) Some of the  
 452 landslides identified by optical images are historically deformed areas that were stable during the InSAR  
 453 observation period, which is beyond the scope of InSAR mapping.



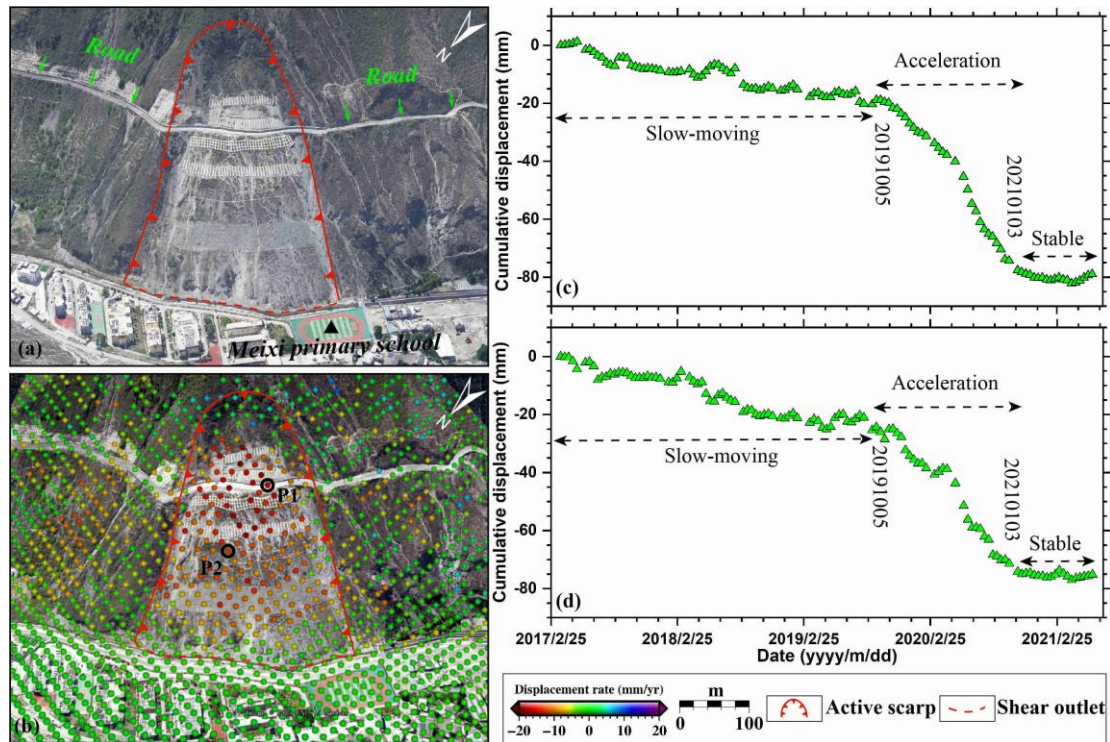
454

455 **Fig. 9.** Spatial distribution and qualitative comparison of landslides detected by InSAR (a) and optical images  
 456 (b). The black line indicates the national highway and the blue lines are the rivers.

## 457 **4.4 Deformation patterns of different types of landslides**

### 458 *4.4.1 Slide movement type*

459 The Meixi Primary School landslide was selected as the study site to investigate the deformation patterns  
460 of the slide movement type, which was placed on the eastern slope of the Meixi Primary School in the town of  
461 Deqin County (No.6, marked in Fig. 8). Figure 10(a) shows an optical image obtained from the UAV  
462 measurements in September 2020. The field geological survey demonstrated that the landslide had an average  
463 thickness of 10 m, with a volume of approximately  $52 \times 10^4 \text{ m}^3$  and a slope angle of  $55 \sim 60^\circ$ , and it belonged  
464 to the category of moderate-scale rock landslides. As shown in Fig. 10(a), the boundary of the active scarp  
465 (approximately 1–2 m in width) of the landslide (solid red line with triangles) is evident, and there is a road  
466 crossing through the head of the landslide. In addition, the entire slope was reinforced using slide-resistant piles  
467 (Fig. 10(a)), thereby increasing the safety factor to some extent. Figure 10(b) shows the LOS displacement rate  
468 from March 2017 to June 2021 superimposed on an optical image. The displacement time series of points P1  
469 and P2 are shown in Figs. 10(c) and (d), respectively. As shown in Fig. 10(b), the active boundary of the slope  
470 delineated from the displacement map perfectly matched that derived from the geomorphological analysis of  
471 the UAV image, and the entire landslide was active during the InSAR observation period. The maximum  
472 displacement rate in the LOS direction is 19 mm/y. The displacement time series presented in Figs. 10(c) and  
473 (d) illustrate the nonlinear displacement trend of the slope from March 2017 to June 2021. The landslide moved  
474 slowly from March 25, 2017, to October 5, 2019, followed by a significantly accelerated displacement from  
475 October 5, 2019, to January 3, 2021, and entered a nearly stable state after January 3, 2021. Evidence from field  
476 investigations suggests that landslide stability is affected by external factors such as rainfall, earthquakes, and  
477 freeze-thaw action. In particular, the earthquake increased the activity in August 2018. The accelerated  
478 displacement started in October 2019; thus, we infer that the freeze-thaw action may have triggered such an  
479 abnormal displacement.



480

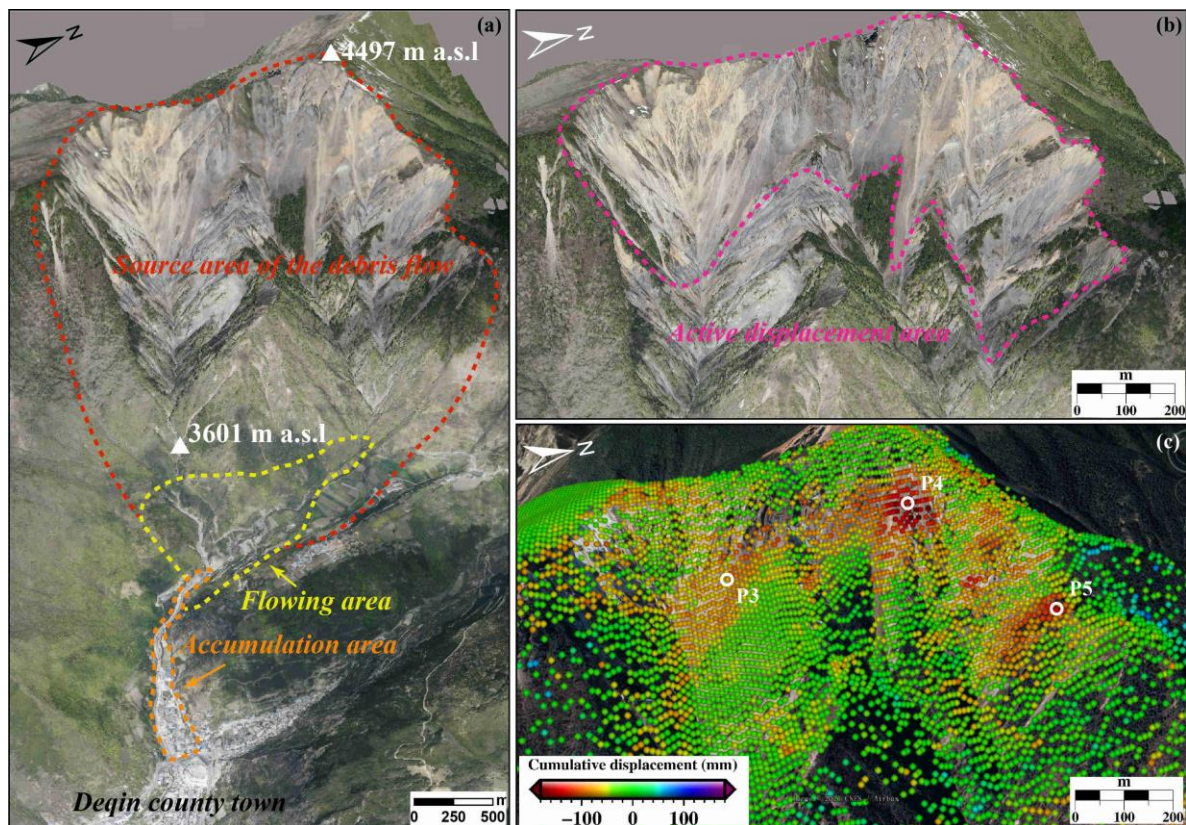
481 **Fig. 10.** Optical image and displacement map of the Meili primary school landslide. (a) UAV image acquired  
 482 in September 2020; (b) LOS displacement rate obtained with descending Sentinel-1 images from March 2017  
 483 to June 2021; (c) InSAR displacement time series of point P1 marked in (b); and (d) InSAR displacement time  
 484 series of point P2 marked in (b).

#### 485 4.4.2 Flow movement type

486 We selected the Zhixi River debris flow, labeled No.7 in Fig. 8 and Table 1, as the study site to investigate  
 487 the deformation patterns of the flow movement type. Figure 11(a) shows the full view and landform features of  
 488 the Zhixi River debris flow using a UAV image acquired in September 2020, whereas Fig. 11(b) shows an  
 489 amplified UAV image of the active displacement area of the debris flow derived from InSAR measurements.  
 490 The debris flow covered a basin area of approximately 6.38 km<sup>2</sup> and was composed of three parts: the source  
 491 area (5.35 km<sup>2</sup>), flowing area (1.78 km<sup>2</sup>), and accumulation area (0.25 km<sup>2</sup>), as shown in Fig. 11(a) by dotted  
 492 polygons with different colors. The highest altitude of the debris flow was 4497 m a.s.l., and the lowest altitude  
 493 was 3365 m a.s.l., thus forming a relative elevation of 1130 m, which provides great potential energy for rupture.  
 494 As shown in Figs. 11 (a) and (b), extensive collapse and disruption occurred in the trailing section of the debris  
 495 flow, suggesting that the debris flow was in a critical equilibrium state. The displacement map retrieved from



496 ascending Sentinel-1 images (Fig. 11(c)) revealed that the maximum cumulative displacement between April  
497 2017 and May 2021 reached -192 mm in the LOS direction, and the displacement was merely detected in areas  
498 where surface disruption occurred. Thus, these InSAR results enable the identification of active displacement  
499 areas and provide information about their deformation magnitude, which is paramount for risk assessment of  
500 debris flows.

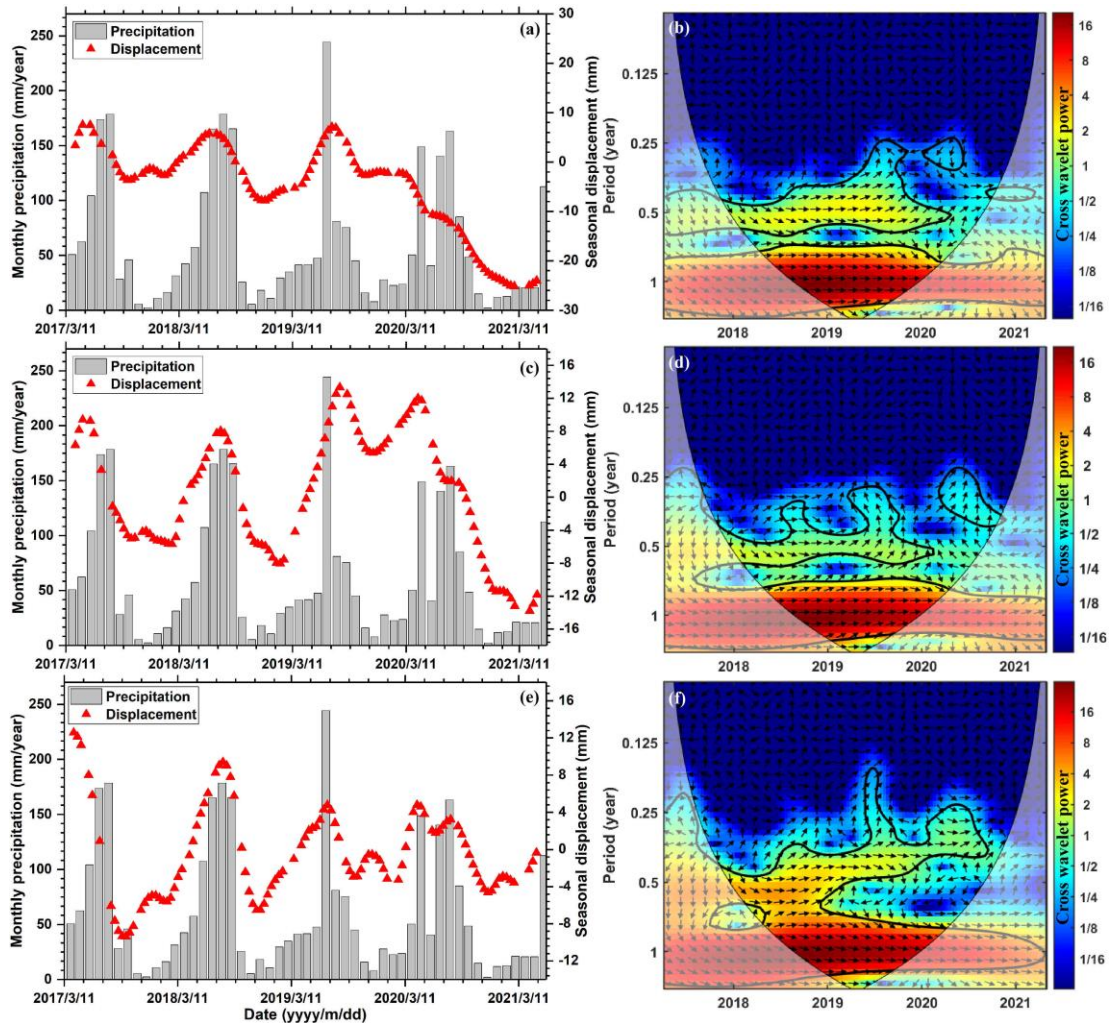


502 **Fig. 11.** Zhixi River debris flow, labeled as No. 7 in Fig. 8 and Table 1. (a) UAV image showing full view and  
503 landform features of the debris flow; (b) Enlarged UAV image of the active displacement area derived from  
504 InSAR measurements; and (c) LOS cumulative displacement from April 2017 to May 2021.

505 We selected three points, P3-P5, located in different areas of the Zhixi River debris flow, as indicated by  
506 white circles in Fig. 11(c), to analyze the temporal evolution characteristics. The original InSAR displacement  
507 time series for the three points is shown in Fig. S3(a), S4(a), and S5(a), respectively. The results suggest that  
508 the debris flow was deformed with a remarkably nonlinear trend during the InSAR observations, which may be  
509 closely correlated with the periodic strong rainfall in the study area. The relationship between slope  
510 displacement and rainfall was quantitatively analyzed using the cross wavelet transform (XWT) tool to confirm

511 how rainfall changes slope kinematics in the study area. The XWT expands the time series of different variables  
512 into a time-frequency domain to intuitively identify the period/frequency of the data (Tomás et al., 2015). First,  
513 the seasonal component of slope displacement was obtained by decomposing the original InSAR displacement  
514 time series using an empirical mode decomposition (EMD) algorithm (Huang et al., 1998). EMD is a data-  
515 driven method that can decompose a non-stationary time series into several intrinsic mode functions (IMF) and  
516 one trend component without the need to select parameters. Figures S3(b)–(d), S4(b)–(d), and S5(b)–(d) show  
517 the decomposed intrinsic mode functions (IMF1 and IMF2) and trend components (residual) for points P3, P4,  
518 and P5, respectively. Here, IMF1 may be related to noise, IMF2 can be interpreted as the seasonal slope  
519 displacement and was selected for further analysis, and the residual describes the long-term, nearly linear  
520 deformation of the slope.

521 Figure 12 shows the XWT seasonal slope displacement (IMF2) analyses at points P3-P5 and the monthly  
522 precipitation. As shown in Figs. 12 (a), (c), and (e), the rainfall peaks appear in the summer from July to  
523 September, and the slope displacement oscillations are closely correlated with seasonal changes in rainfall.  
524 Figure 12 (b), (d), and (f) illustrate the highly common power spectrum between the displacement time series  
525 and rainfall during the one-year period for the three points during the InSAR observation period (i.e., from April  
526 2017 to May 2021). Additionally, we observed a common power with a period of approximately six months at  
527 the three points. As expected, the slope displacement time series were in phase, with high monthly precipitation  
528 in the sections with substantial common power; that is, the phase shifts were approximately equal to zero, as  
529 indicated by the black arrows pointing towards the right in Figs. 12 (b), (c), and (d). This reveals that there was  
530 no significant delay in the time between the onset of slope deformation and the arrival of heavy rainfall.  
531 Moreover, in some time periods, accelerated displacement occurs ahead of reaching the rainfall peak. This  
532 means that the slope displacement tends to accelerate when precipitation exceeds the intensity–duration  
533 threshold rather than the arrival of the rainwater peak. Consequently, we can conclude that the kinematics of  
534 the Zhixi River debris flows are highly conditioned by seasonal precipitation. Periodic heavy rainfall changes  
535 the equilibrium conditions of the slope, thereby generating periodicity in the displacement time series. Therefore,  
536 InSAR analysis has enabled the identification of the most likely triggering factor for the debris flow activity in  
537 the Zhixi River. This relationship is paramount for efficient scientific management of this hazard.



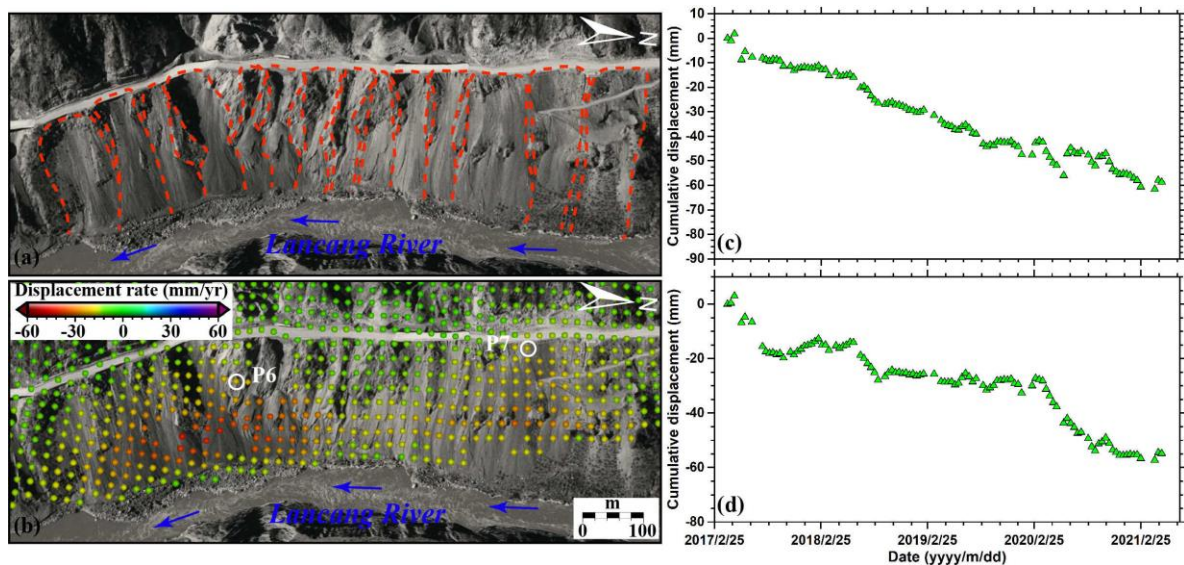
538

539 **Fig. 12.** Power spectra of cross wavelet transform (XWT) of slope seasonal displacement and monthly  
540 precipitation at points P3–P5 labeled in Fig. 11 (c). (a), (c), and (e) are the seasonal displacement time series  
541 for points P3, P4, and P5, respectively; and (b), (d), and (f) are the XWT power spectra of slope displacement  
542 and precipitation at points P3, P4, and P5, respectively.

#### 543 4.4.3 Fall movement type

544 An example of the fall movement type is shown in Fig. 13, which is located on the right bank of the  
545 Lancang River (labelled No. 8 in Fig. 8), named the Xidang earth-fall group. Figure 13(a) shows the optical  
546 remote sensing image of the earthfall group, Fig. 13(b) shows the displacement rate acquired from the ascending  
547 Sentinel-1 between April 2017 and May 2021, and Figs. 13(c) and (d) show the displacement time series of  
548 points P6 and P7, marked in Fig. 13(b). As shown in Fig. 13(a), the earthfall group comprises several smaller  
549 earthfalls. Many small superficial secondary failures, as well as active earthfall channels can also be clearly

550 observed in the optical image, implying the ongoing activity of the slope. A clear displacement is visible in the  
551 entire earthfall group, and the corresponding displacement shown in Fig. 13(b) indicates that the maximum  
552 displacement velocity reached -42 mm/year between April 2017 and May 2021. On the other hand, a nearly  
553 linear displacement trend was found in the time series presented in Fig. 13(c); however, nonlinear displacement  
554 characteristics were observed in the time series shown in Fig. 13(d).



555  
556 **Fig. 13.** Optical image and displacements map of the Xidang earth-fall group, labeled as No. 8 in Fig. 8. (a)  
557 Google Earth image, the red dotted lines indicate the boundary of earth fall; (b) LOS displacement rate estimated  
558 with ascending Sentinel-1 images from April 2017 to May 2021; (c) InSAR displacement time series of point  
559 P6 marked in (b); and (d) InSAR displacement time series of point P7 marked in (b).

## 560 5. Discussion

### 561 5.1 Statistical assessment of the performance of the proposed atmospheric correction method

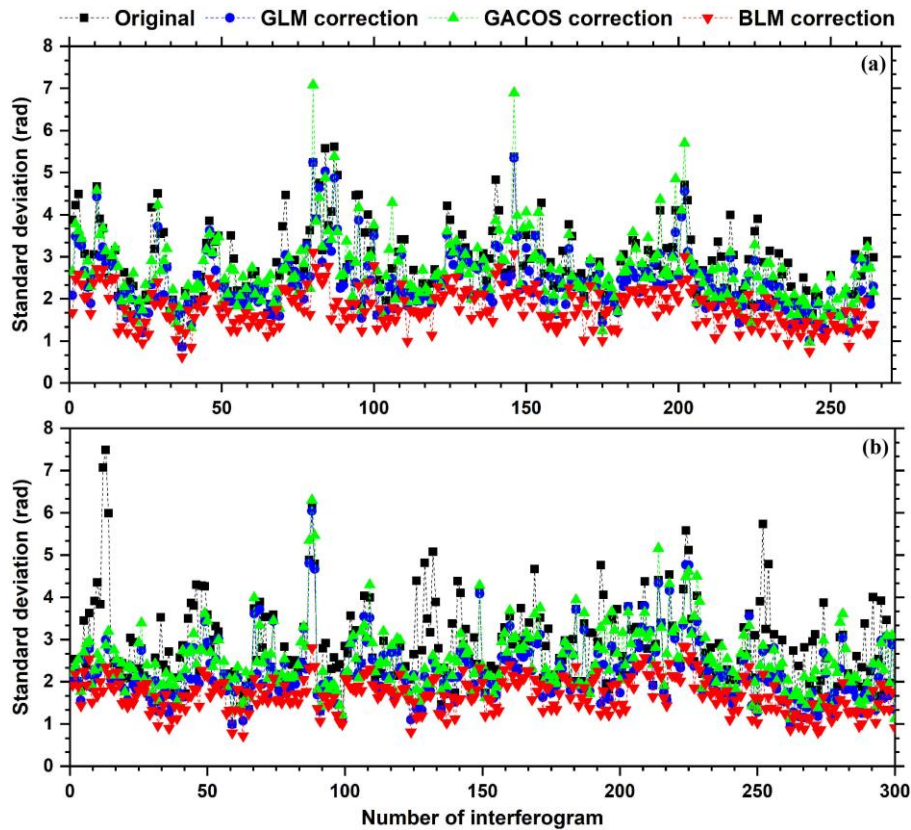
562 Several metrics have been proposed in the literature (Albino et al., 2020; Yu et al., 2018) for evaluating  
563 the performance of the tropospheric delay correction method: i) the standard deviation (STD) of the individual  
564 interferogram, ii) the STD of the estimated displacement, iii) the reduction in the STD after correction, and iv)  
565 the internal cross-comparison between the results corrected by different methods. As there were no data from  
566 in situ measurements, the metrics mentioned above were exploited to assess the effectiveness and performance  
567 of the proposed atmospheric correction method in terms of individual interferograms, as well as the estimated  
568 displacement rate and time series.

### 569 5.1.1 Corrections to interferograms

570 Phase-based models (i.e., the GLM approach) and GACOS products have been widely used to correct  
571 InSAR tropospheric delays in landslide mapping over wide regions (Liu et al., 2021a; Shi et al., 2019; Yu et al.,  
572 2018). Therefore, we employed the GLM approach and GACOS products for comparison with the proposed  
573 method, and atmospheric delays in the interferograms were independently corrected using the three methods.  
574 The STD for the 565 unwrapped interferograms was calculated from the ascending and descending images  
575 before and after atmospheric correction, as shown in Fig. 14. Owing to the phase errors related to the  
576 unwrapping error, the orbital and DEM errors were correctly compensated for in the InSAR processing; thus,  
577 the STD can directly reflect the magnitude of the atmospheric delay. It can be observed from Fig. 14 that the  
578 STDs of the original interferogram are characterized by seasonal variation, which has also been demonstrated  
579 by previous studies in steep terrains (Doin et al., 2009). As for the ascending interferograms, the GACOS  
580 products successfully corrected 151 interferograms, accounting for approximately 57% of all interferograms,  
581 whereas the GLM method reduced the STD by 97% of all interferograms (255 in number). Similar results were  
582 obtained for the descending interferograms; approximately 58% (175 in number) of all interferograms were  
583 improved by the GACOS products, and 98% (294 in number) of all interferograms were corrected using the  
584 GLM approach. Moreover, the GACOS products introduce large uncertainties into some interferograms (e.g.,  
585 the 80th interferogram in Fig. 14(a)) and increase their STD. In comparison, the atmospheric delays in all  
586 interferograms were efficiently corrected by the proposed method, which can be illustrated by two aspects: 1)  
587 the interferograms corrected by the proposed approach had the smallest STD, and 2) the proposed approach  
588 largely suppressed the seasonal characteristics of the STD. The STD of original interferograms was reduced by  
589 34% on average for the ascending track and 35% on average for the descending track after atmospheric  
590 correction using the proposed method.

591 Fig. S6 shows a 12-day original unwrapped interferogram derived from descending images on June 29,  
592 2017, and July 11, 2017, and the ones corrected by the GLM approach, GACOS products, and the proposed  
593 approach. The original interferograms (Fig. S6(a)) exhibited an STD of 2.26 rad and part of the signal correlated  
594 with the topography. The tropospheric delay primarily consisted of large positive LOS changes in the eastern  
595 part of the study area. We can see from Fig. S6(b) that the GACOS approach showed the poorest performance  
596 in correcting the atmospheric signals in this interferogram. The STD decreases to 1.62 rad after the GLM  
597 correction (Fig. S6(c)). However, the correction introduced positive LOS changes along the Lancang River. In

598 contrast, the proposed method (i.e., the BLM method) corrected atmospheric artifacts very well and decreased  
599 the STD to 1.17 rad (Fig. S6(d)). This example demonstrates that the proposed method outperforms the GACOS  
600 and GLM methods.

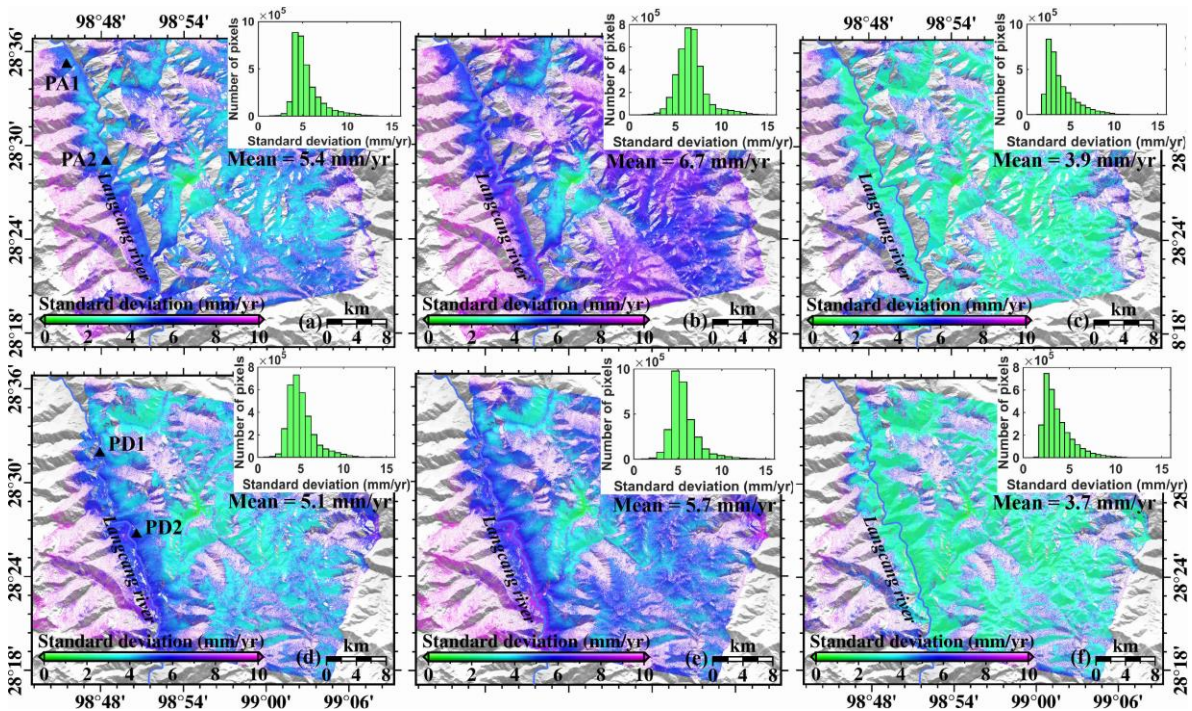


601  
602 **Fig. 14.** The standard deviations (STDs) of the original unwrapped interferogram and those corrected by the  
603 GLM approach, GACOS products, and the BLM approach. (a) Ascending interferograms, and (b) descending  
604 interferograms.

### 605 5.1.2 Accuracy improvement in displacement rate

606 The precision of the InSAR-derived displacement rate is crucial for highly accurate landslide detection.  
607 The inner precision (or measurement uncertainty) of the displacement rate is reflected by the standard deviation.  
608 To assess the accuracy improvement of our proposed method in terms of the displacement rate, the STDs of the  
609 displacement rates derived from the GLM, GACOS, and BLM corrections were computed using Eq (10) from  
610 [Fattahi and Amelung \(2015\)](#), as shown in [Fig. 15](#). It is evident from [Fig. 15](#) that the STDs of both the ascending  
611 and descending displacement rates obtained with the GLM and GACOS corrections were greater than those  
612 derived from the proposed method. For the ascending track, the mean STD derived from the proposed approach  
613 is 3.9 mm/year ([Fig. 15\(c\)](#)), which is greatly smaller than the 5.4 mm/year obtained from the GLM method ([Fig.](#)

614 15(a)), and the 6.7 mm/year obtained from the GACOS correction (Fig. 15(b)). For the descending track, the  
615 mean STD obtained from the proposed method is 3.7 mm/year (Fig. 15(f)), which is also lower than the 5.1  
616 mm/year derived from the GLM method (Fig. 15(d)), and the 5.7 mm/year derived from the GACOS correction  
617 (Fig. 15(e)). Thus, we can conclude that the proposed method improves the inner precision of both the ascending  
618 and descending displacement rates by approximately 27% and 35% with respect to the GLM method and the  
619 GACOS products, respectively.

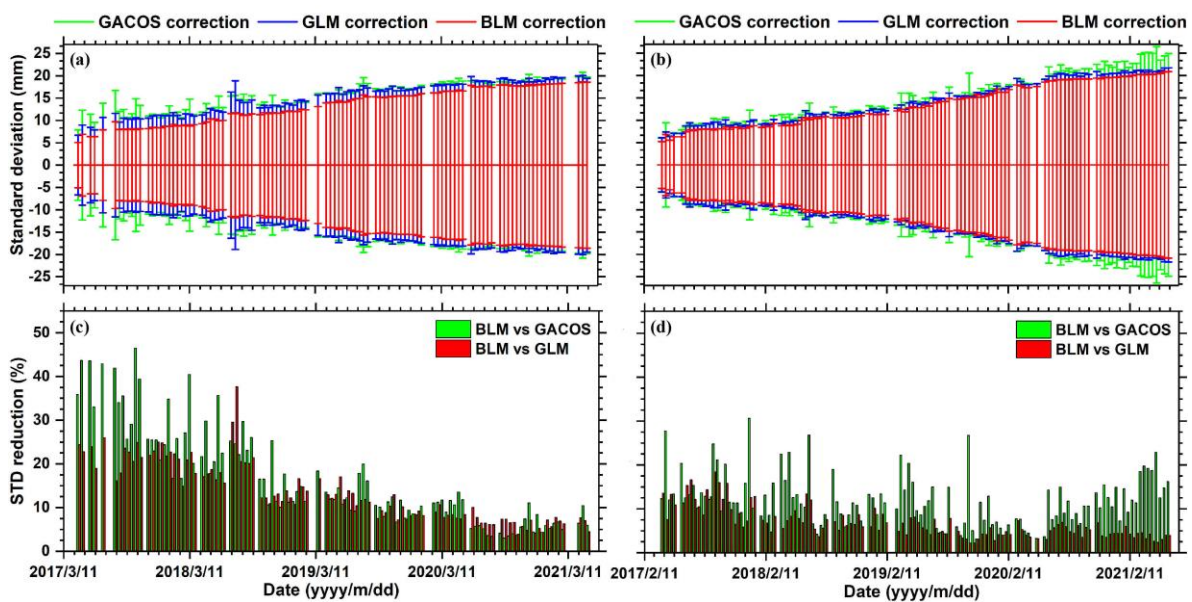


620  
621 **Fig. 15.** Comparison of the standard deviation (STD) of the displacement rates derived from atmospheric  
622 corrections with three different methods. (a), (b) and (c) are the STDs of the ascending displacement rate  
623 calculated with GLM, GACOS, and BLM corrections, respectively; and (d), (e), and (f) are the STDs of the  
624 descending displacement rate calculated with GLM, GACOS and BLM corrections, respectively.

### 625 5.1.3 Accuracy improvement in displacement time series

626 Atmospheric delay can contaminate the InSAR-derived displacement time series and thus may misinterpret  
627 the temporal evolution of landslide movements and generate false signals in early warning. To assess the  
628 improvement in the accuracy of our proposed approach in the estimated displacement time series, we calculated  
629 the global standard deviation (GSTD) (Albino et al., 2020) of the ascending and descending displacement time  
630 series derived from the GLM, GACOS, and BLM atmospheric corrections, as shown in Fig. 16(a) and (b). In

631 addition, we calculated the reduction percentages in the GSTD of the proposed approach with respect to the  
632 GACOS and GLM corrections, as shown in Fig. 16(c) and (d). Overall, Fig. 16 shows that the displacement  
633 time series derived from the proposed approach has the smallest GSTD compared to those derived from the  
634 other two methods. For the ascending track, the largest reductions in GSTD of the proposed approach are 46.5%  
635 and 37.7%, respectively, with respect to the GACOS and GLM corrections. For the descending track, the largest  
636 reductions in GSTD of the proposed approach were 30.6% and 18.4%, respectively. This illustrates that the  
637 proposed method is significantly more effective at correcting atmospheric artifacts than the other two methods.

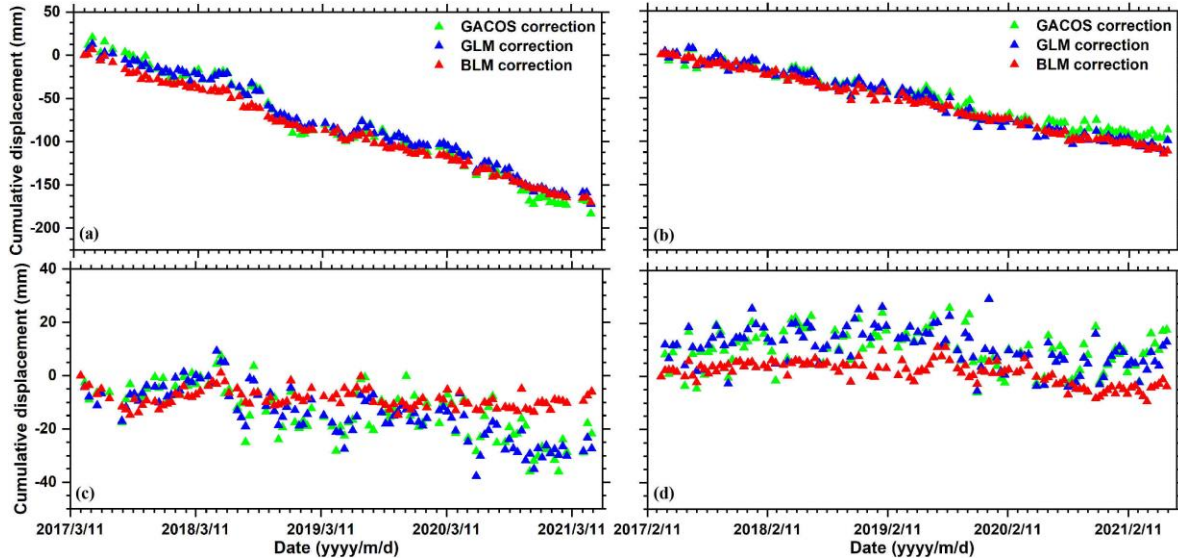


638  
639 **Fig. 16.** Comparison of the global standard deviation (GSTD) of the displacement time series calculated with  
640 the GACOS, GLM, and BLM corrections. (a) and (b) are the GSTDs of the ascending and descending  
641 displacement time series, respectively, and (c) and (d) are the GSTD reduction percentages of the proposed  
642 method relative to the other two methods for the ascending and descending tracks, respectively.

643 Moreover, the displacement time series of the ascending and descending tracks derived from the GACOS,  
644 GLM, and BLM methods were extracted at points PA1-PA2 and PD1-PD2 (Fig. 15(a) and (d)) to further  
645 demonstrate the proposed method, as shown in Fig. 17. Points PA1 and PD1 were placed in two landslide  
646 regions, whereas points PA2 and PD2 were located in stable regions. As shown in Fig. 17, the displacement  
647 time series obtained from the GACOS and GLM corrections exhibit pronounced seasonal oscillations,  
648 particularly at PA2. The smallest oscillations occurred in January and February, while the largest were observed  
649 in July and August. As expected, seasonal oscillations were eliminated from the displacement time series after



650 the BLM correction, and the cumulative displacements at points PA2 and PD2 were closer to zero. This result  
651 suggests that it is essential to remove undesired atmospheric artifacts before interpreting InSAR-derived  
652 landslide displacement.



653  
654 **Fig. 17.** Displacement time series for the points PA1-PA2 and PD1-PD2 (marked in Fig. 15(a) and (d))  
655 calculated with the GACOS, GLM, and BLM corrections. (a) and (c) are points PA1 and PA2 from the  
656 ascending Sentinel-1 images, respectively; and (b) and (d) are points PD1 and PD2 from the descending  
657 Sentinel-1 images, respectively.

## 658 5.2 Advantages and drawbacks of the proposed method

659 Considering the complex geomorphic and environmental conditions of high mountainous terrains, we first  
660 developed a block-based linear model to efficiently correct tropospheric delays and generate high-accuracy  
661 displacement maps. We then developed a semi-automatic approach to map and classify different types of  
662 landslides. The approach developed in this study can be extended to other high mountainous terrains. For  
663 example, the loss of human lives and infrastructure is frequently caused by catastrophic landslides in the  
664 Himalayan region owing to tectonic activity, extreme precipitation, steep topography, high altitude, and intense  
665 human activity. However, a comprehensive inventory map of catastrophic landslides in this region is lacking  
666 because of the complicated geomorphology and environmental conditions. The proposed refined InSAR method  
667 can generate high-accuracy ground deformation rate and time series for the Himalayas. The proposed semi-  
668 automatic approach allows for fast and efficient large-area landslide inventory mapping based on InSAR-

669 derived deformation maps, thereby contributing to a comprehensive assessment of the risks associated with  
670 landslide events. The advantages of the proposed atmospheric correction method are highlighted in [Section 5.1](#)  
671 by comparing two extensively used atmospheric correction methods. Compared with the GACOS products, the  
672 proposed approach does not require any external weather model and thus can avoid the uncertainties caused by  
673 the low spatiotemporal resolution of external weather models ([Figs. 14](#) and [S6](#)). Unlike the classical phase-  
674 based linear model, the proposed approach considers the spatial and seasonal variations of tropospheric  
675 properties and overcomes the influences of unwrapping error and ground deformation on parameter estimation.  
676 However, the proposed approach still suffers from two drawbacks: (1) It is suitable for correcting the  
677 atmospheric delay of localized deformation signals, such as those caused by landslides and land subsidence,  
678 and is inapplicable to scenarios with long-wavelength deformation signals, such as those caused by tectonic  
679 activities; and (2) the estimated tropospheric delays can be affected by the quality of phase unwrapping, that is,  
680 the numerous unwrapping errors in extremely low-coherence scenarios can lead to uncertainties in the estimated  
681 delay. The second drawback can be addressed to some extent by employing more robust phase-unwrapping  
682 algorithms (e.g., 3D phase-unwrapping) in low-coherence scenarios. The proposed BLM approach can be  
683 further improved by adaptively selecting an appropriate block size.

684 In most previous studies ([Shi et al., 2019](#)), only the InSAR-derived displacement rate has been used to  
685 identify landslides over wide regions. The average displacement rate presents an important clue for identifying  
686 landslides with linear movement patterns; however, this may omit landslides with nonlinear or cyclic patterns  
687 of motion. The proposed approach overcomes this issue by simultaneously employing InSAR-derived  
688 displacement rates and time-series data. Furthermore, to ensure the high reliability and accuracy of the detected  
689 landslides, mistaken and isolated pixels were automatically removed from the estimated deformation maps  
690 through a preprocessing procedure. Although our proposed approach does its best to improve the accuracy and  
691 reliability of landslide detection, some active landslides may have been omitted because of the limited resolution  
692 of Sentinel-1 images, the influence of SAR geometrical distortions, and the decorrelations caused by vegetation,  
693 ice, and snow cover, as well as rapid deformation. These drawbacks can be eliminated by employing multi-  
694 wavelength SAR datasets and multiple types of SAR and InSAR methods for landslide mapping in high-  
695 mountain terrain. For example, high-resolution SAR images such as TerraSAR-X have a strong ability to detect  
696 small-scale landslides. The decorrelation caused by covers of vegetation and ice and snow can be solved using  
697 long-wavelength SAR images such as ALOS/PALSAR-2 and LuTan-1, and the phase decorrelation caused by

698 rapid landslide movement can be solved using the SAR offset-tracking method (Liu et al., 2020). In addition,  
699 the detected landslides are generally divided into categories of falls, slides, and flows according to the type of  
700 movement. Detailed categorization was not performed owing to the lack of fine-scale geological information,  
701 such as the slope material and mechanical characteristics of the slide zone. The inventory map for the three  
702 landslide types could be updated using fine-scale geological information in conjunction with field investigations.  
703

## 704 **6 Conclusion**

705 The occurrence of catastrophic landslide hazards is of great concern to natural hazards and  
706 geomorphological sciences, particularly in high-mountain regions. Generally, InSAR can accurately measure  
707 landslide displacements across wide regions. However, its accuracy is significantly reduced in high mountain  
708 environments with extremely rugged terrain, dense vegetation, and snow, such as in our study area. This is due  
709 to the coupling effects of severe atmospheric artifacts and decorrelation noise. To address these limitations and  
710 broaden the application of InSAR in landslide investigations, in this study, we propose a refined InSAR method  
711 that was applied in Deqin County to map and classify the displacements of different landslide types. First, a  
712 block-based linear model (BLM) was used to estimate and correct atmospheric delays by considering the spatial  
713 variability of tropospheric properties, allowing us to compute high-precision InSAR displacement maps. Based  
714 on InSAR-derived displacements and DEM-derived C-index maps, a semi-automatic procedure for the mapping  
715 and classification of different types of landslides was developed. The outcomes of this analysis provide  
716 important data for the risk assessment of geohazards in Deqin County. The primary findings are summarized as  
717 follows:

718 (1) The proposed BLM method efficiently corrects tropospheric delays in InSAR interferograms without  
719 using auxiliary data. Comparisons of the BLM approach with the GLM and GACOS approaches illustrate its  
720 superiority for individual interferograms and estimated displacements. The inner precision of the displacement  
721 rate was improved by more than 27% after the BLM correction.

722 (2) The displacement maps retrieved from ascending and descending Sentinel-1 images revealed that there  
723 is a total of 317 landslide hazards in the study area, including 34 slides, 25 falls, and 258 flows. The reliability  
724 of the active landslides detected by InSAR was qualitatively evaluated using an a priori inventory map derived  
725 from the visual interpretation of satellite and UAV images and field geological surveys. Some previously

726 unknown landslides were identified in this study, and the active boundaries of some landslides were accurately  
727 delimited using InSAR.

## 728 **Acknowledgments**

729 This research was financially supported by the Natural Science Foundation of China (Grant No. 41929001)  
730 and National Key R&D Program of China (No.2022YFC3004302). This research was also supported by a  
731 Chinese Scholarship Council studentship awarded to Xiaojie Liu (Ref. 202006560031), the Science Foundation  
732 of Gansu Province (Nos. 23JRRA830 and 23ZDFA007), and the ESA-MOST China DRAGON-5 project (ref.  
733 59339). The Sentinel-1 images were freely provided by European Space Agency (ESA) and downloaded from  
734 <https://search.asf.alaska.edu/#/>. We thank the editors and three anonymous reviewers for constructive comments  
735 that improved the paper.

## 736 **References**

- 737 Albino, F., Biggs, J., Yu, C., Li, Z.H., 2020. Automated Methods for Detecting Volcanic Deformation Using  
738 Sentinel-1 InSAR Time Series Illustrated by the 2017–2018 Unrest at Agung, Indonesia. *Journal of*  
739 *Geophysical Research: Solid Earth* 125(2), e2019JB017908.
- 740 Barnhart, W.D., Lohman, R.B., 2013. Characterizing and estimating noise in InSAR and InSAR time series  
741 with MODIS. *Geochemistry Geophysics Geosystems* 14, 4121–4132.
- 742 Barra, A., Solari, L., Béjar-Pizarro, M., Monserrat, O., Bianchini, S., Herrera, G., Crosetto, M., Sarro, R.,  
743 González-Alonso, E., Mateos, R., Ligüerzana, S., López, C., Moretti, S., 2017. A Methodology to Detect  
744 and Update Active Deformation Areas Based on Sentinel-1 SAR Images. *Remote Sensing* 9(10), 1002.
- 745 Bekaert, D.P.S., Hooper, A., Wright, T.J., 2015. Reassessing the 2006 Guerrero slow-slip event, Mexico:  
746 Implications for large earthquakes in the Guerrero Gap. *Journal of Geophysical Research: Solid Earth*  
747 120(2), 1357-1375.

- 
- 748 Berardino, P., Fornaro, G., Lanari, R., Sansosti, E., 2002. A new algorithm for surface deformation monitoring  
749 based on small baseline differential SAR interferograms. *IEEE Transactions on Geoscience and Remote*  
750 *Sensing* 40(11), 2375-2383.
- 751 Costantini, M., 1998. A novel phase unwrapping method based on network programming. *IEEE Transactions*  
752 *on Geoscience and Remote Sensing* 36(3), 813-821.
- 753 Crippa, C., Valbuzzi, E., Frattini, P., Crosta, G.B., Spreafico, M.C., Agliardi, F., 2021. Semi-automated regional  
754 classification of the style of activity of slow rock-slope deformations using PS InSAR and SqueeSAR  
755 velocity data. *Landslides* 18(7), 2445-2463.
- 756 Doin, M.P., Lasserre, C., Peltzer, G., Cavalié, O., Doubre, C., 2009. Corrections of stratified tropospheric delays  
757 in SAR interferometry: Validation with global atmospheric models. *Journal of Applied Geophysics* 69(1),  
758 35-50.
- 759 Ferretti, A., Prati, C., Rocca, F., 2001. Permanent Scatterers in SAR Interferometry. *IEEE Transactions on*  
760 *Geoscience and Remote Sensing* 39(1), 8-20.
- 761 Fattahi, H., Amelung, F., 2015. InSAR bias and uncertainty due to the systematic and stochastic tropospheric  
762 delay. *J. Geophys. Res.: Solid Earth* 120 (12), 8758-8773.
- 763 Gariano, S.L., Guzzetti, F., 2016. Landslides in a changing climate. *Earth-Science Reviews* 162, 227-252.
- 764 Goldstein, R.M., Werner, C.L., 1998. Radar interferogram filtering for geophysical applications. *Geophysical*  
765 *Research Letters* 25(21), 4035-4038.

- 
- 766 Handwerger, A.L., Booth, A.M., Huang, M.H., Fielding, E.J., 2021. Inferring the subsurface geometry and  
767 strength of slow-moving landslides using 3-D velocity measurements from the NASA/JPL UAVSAR.  
768 *Journal of Geophysical Research: Earth Surface* 126(3), e2020JF005898.
- 769 Hock, R., Rasul, G., Adler, C., Cáceres, B., Gruber, S., Hirabayashi, Y., et al., 2019. High mountain areas. In  
770 H.-O. Pörtner, D. C. Roberts, V. Masson-Delmotte, P. Zhai, M. Tignor, E. Poloczanska, et al. (Eds.).  
771 IPCC Special Report on the Ocean and Cryosphere in a Changing Climate, pp. 131-202.
- 772 Huber, P.J., 1964. Robust estimation of a location parameter. *The Annals of Mathematical Statistics* 35(1), 73–  
773 101.
- 774 Hungr, O., Leroueil, S., Picarelli, L., 2013. The Varnes classification of landslide types, an update. *Landslides*  
775 11(2), 167-194.
- 776 Jin, J.C., Chen, G., Meng, X.M., Zhang, Y., Shi, W., Li, Y.X., Yang, Y.P., Jiang, W.Y., 2022. Prediction of  
777 river damming susceptibility by landslides based on a logistic regression model and InSAR techniques: A  
778 case study of the Bailong River Basin, China. *Engineering Geology* 299, 106562.
- 779 Li, Z.H., Fielding, E.J., Cross, P., Muller, J.-P., 2006. Interferometric synthetic aperture radar atmospheric  
780 correction: Medium Resolution Imaging Spectrometer and Advanced Synthetic Aperture Radar integration.  
781 *Geophysical Research Letters* 33(6), L06816.
- 782 Liang, H.Y., Zhang, L., Ding, X.L., Lu, Z., Li, X., 2019. Toward Mitigating Stratified Tropospheric Delays in  
783 Multitemporal InSAR: A Quadtree Aided Joint Model. *IEEE Transactions on Geoscience and Remote*  
784 *Sensing* 57(1), 291-303.

- 
- 785 Liu, X.J., Zhao, C.Y., Zhang, Q., Lu, Z., Li, Z.H., 2020. Deformation of the Baige Landslide, Tibet, China,  
786 Revealed Through the Integration of Cross-Platform ALOS/PALSAR-1 and ALOS/PALSAR-2 SAR  
787 Observations. *Geophysical Research Letters* 47(3), e2019GL086142.
- 788 Liu, X.J., Zhao, C.Y., Zhang, Q., Lu, Z., Li, Z.H., Yang, C.S., Zhu, W., Liu-Zeng, J., Chen, L.Q., Liu, C.J.,  
789 2021a. Integration of Sentinel-1 and ALOS/PALSAR-2 SAR datasets for mapping active landslides along  
790 the Jinsha River corridor, China. *Engineering Geology* 284, 106033.
- 791 Liu, X.J., Zhao, C.Y., Zhang, Q., Yin, Y.P., Lu, Z., Samsonov, S., Yang, C.S., Wang, M., Tomás, R., 2021b.  
792 Three-dimensional and long-term landslide displacement estimation by fusing C- and L-band SAR  
793 observations: A case study in Gongjue County, Tibet, China. *Remote Sensing of Environment* 267, 112745.
- 794 Mani, P., Allen, S., Evans, S., Kargel, J., Mergili, M., Petrakov, D., Stoffel, M., 2023. Geomorphic process  
795 chains in high-mountain regions-A review and classification approach for natural hazards assessment.  
796 *Reviews of Geophysics* 61, e2022RG000971.
- 797 Roback, K., Clark, M. K., West, A. J., Zekkos, D., Li, G., Gallen, S. F., et al. (2018). The size, distribution,  
798 and mobility of landslides caused by the 2015 Mw7. 8 Gorkha earthquake, Nepal. *Geomorphology* 301,  
799 121-138.
- 800 Shi, X.G., Yang, C., Zhang, L., Jiang, H.J., Liao, M.S., Zhang, L., Liu, X.G., 2019. Mapping and characterizing  
801 displacements of active loess slopes along the upstream Yellow River with multi-temporal InSAR datasets.  
802 *Sci. Total. Environ.* 674, 200-210.
- 803 Shugar, D.H., Jacquemart, M., Shean, D., et al., 2021. A massive rock and ice avalanche caused the 2021  
804 disaster at Chamoli, Indian Himalaya. *Science* 2021, 373(6552), 300-306.

- 
- 805 Tomás, R., Pagán, J.I., Navarro, J.A., Cano, M., Pastor, J.L., Riquelme, A., Cuevas-González, M., Crosetto, M.,  
806 Barra, A., Monserrat, O., Lopez-Sanchez, J.M., Ramón, A., Ivorra, S., Soldato, M.D., Solari, L., Bianchini,  
807 S., Raspini, F., Novali, F., Ferretti, A., Costantini, M., Trillo, F., Herrera, G., Casagli, N., 2019. Semi-  
808 automatic identification and pre-screening of geological–geotechnical deformational processes using  
809 persistent scatterer interferometry datasets. *Remote Sensing* 11(14), 1675.
- 810 Varnes, D.J., 1978. Slope movement types and processes. In: Schuster RL, Krizek RJ (eds) *Landslides, analysis*  
811 *and control*, special report 176: Transportation research board, National Academy of Sciences, Washington,  
812 DC., pp. 11–33.
- 813 Wegmuller, U., Werner, C., 1997. Gamma SAR processor and interferometry software. The 3rd ERS  
814 symposium on space at the service of our environment 414, 1687-1692.
- 815 Xie, M.L., Zhao, W. H., Ju, N.P., He, C.Y., Huang, H.D., Cui, Q. H., 2020. Landslide evolution assessment  
816 based on InSAR and real-time monitoring of a large reactivated landslide, Wenchuan, China. *Engineering*  
817 *Geology* 277, 105781.
- 818 Xu, Q., Guo, C., Dong, X.J., Li, W.L., Lu, H.Y., Fu, H., Liu, X.S., 2021. Mapping and Characterizing  
819 Displacements of Landslides with InSAR and Airborne LiDAR Technologies: A Case Study of Danba  
820 County, Southwest China. *Remote Sensing* 13(21), 4234.
- 821 Yu, C., Li, Z.H., Penna, N.T., Crippa, P., 2018. Generic Atmospheric Correction Model for Interferometric  
822 Synthetic Aperture Radar Observations. *Journal of Geophysical Research: Solid Earth* 123(10), 9202-9222.
- 823 Yu, C., Penna, N.T., Li, Z.H., 2017. Generation of real-time mode high-resolution water vapor fields from GPS  
824 observations. *Journal of Geophysical Research: Atmospheres* 122(3), 2008-2025.



825 Yin, Y., Li, B., Gao, Y., Wang, W., Zhang, S., Zhang, N., 2023. Geostuctures, dynamics and risk mitigation  
826 of high-altitude and long-runout rockslides. *Journal of Rock Mechanics and Geotechnical Engineering*  
827 15(1), 66-101.

828 Zhang, S., Zhang, L. M., Li, X.Y., Xu, Q., 2018. Physical vulnerability models for assessing building damage  
829 by debris flows. *Engineering Geology* 247, 145-158.

830

### 831 **List of Figure Captions**

832

833 **Fig. 1.** (a) Location of the study area and spatial coverage of the Sentinel-1 SAR images, where the white  
834 polygon indicates Deqin County; (b) overview of the study area; and (c) overview of Deqin County town (red  
835 polygon in (b)). The UAV measurement acquired the background image in September 2020, and the polygons  
836 with different colors are the a priori landslide hazards.

837

838 **Fig. 2.** Spatial and temporal baseline plots of the used interferograms for ascending (a) and descending (b)  
839 Sentinel-1 images.

840

841 **Fig. 3.** Technical scheme of refined InSAR method for mapping and classifying active landslides in high  
842 mountain regions where ADAs indicate active displacement areas.

843 **Fig. 4.** Rationale of the block-based linear model for atmospheric correction. Overl. represents the overlapping  
844 region between two adjacent blocks and Wind. Size is the size of each block.

845

846 **Fig. 5.** (a) and (b) are the C-index maps of the study area for the ascending and descending Sentinel-1 images,  
847 respectively; (c) is the C-index map of region A (marked in (a)) for the ascending Sentinel-1 image; and (d) is  
848 the displacement rate of region A calculated using the ascending Sentinel-1 images.

849

850 **Fig. 6.** Knowledge mapping of landslide types, modified from Varnes (1978).

851

852 **Fig. 7.** (a) and (c) show the annual displacement rate and cumulative displacement of the study area derived  
853 from the ascending Sentinel-1 images from April 2017 to May 2021, respectively, and (b) and (d) show the  
854 annual displacement rate and cumulative displacement derived from the descending Sentinel-1 images from  
855 March 2017 to June 2021, respectively.

856

857 **Fig. 8.** Inventory map of active landslides detected by ascending and descending Sentinel-1 images. Note that  
858 the detected landslides were classified according to the classification system of Varnes (1978).

859

860 **Fig. 9.** Spatial distribution and qualitative comparison of landslides detected by InSAR (a) and optical images  
861 (b). The black line indicates the national highway and the blue lines are the rivers.

862

863 **Fig. 10.** Optical image and displacement map of the Meili primary school landslide. (a) UAV image acquired  
864 in September 2020; (b) LOS displacement rate obtained with descending Sentinel-1 images from March 2017  
865 to June 2021; (c) InSAR displacement time series of point P1 marked in (b); and (d) InSAR displacement time  
866 series of point P2 marked in (b).

867

868 **Fig. 11.** Zhixi River debris flow, labeled as No. 7 in [Fig. 8](#) and [Table 1](#). (a) UAV image showing full view and  
869 landform features of the debris flow; (b) Enlarged UAV image of the active displacement area derived from  
870 InSAR measurements; and (c) LOS cumulative displacement from April 2017 to May 2021.

871

872 **Fig. 12.** Power spectra of cross wavelet transform (XWT) of slope seasonal displacement and monthly  
873 precipitation at points P3–P5 labeled in [Fig. 11 \(c\)](#). (a), (c), and (e) are the seasonal displacement time series  
874 for points P3, P4, and P5, respectively; and (b), (d), and (f) are the XWT power spectra of slope displacement  
875 and precipitation at points P3, P4, and P5, respectively.

876

877 **Fig. 13.** Optical image and displacements map of the Xidang earth-fall group, labeled as No. 8 in Fig. 8. (a)  
878 Google Earth image, the red dotted lines indicate the boundary of earth fall; (b) LOS displacement rate estimated  
879 with ascending Sentinel-1 images from April 2017 to May 2021; (c) InSAR displacement time series of point  
880 P6 marked in (b); and (d) InSAR displacement time series of point P7 marked in (b).

881  
882 **Fig. 14.** The standard deviations (STDs) of the original unwrapped interferogram and those corrected by the  
883 GLM approach, GACOS products, and the BLM approach. (a) Ascending interferograms, and (b) descending  
884 interferograms.

885  
886 **Fig. 15.** Comparison of the standard deviation (STD) of the displacement rates derived from atmospheric  
887 corrections with three different methods. (a), (b) and (c) are the STDs of the ascending displacement rate  
888 calculated with GLM, GACOS, and BLM corrections, respectively; and (d), (e), and (f) are the STDs of the  
889 descending displacement rate calculated with GLM, GACOS and BLM corrections, respectively

890  
891 **Fig. 16.** Comparison of the global standard deviation (GSTD) of the displacement time series calculated with  
892 the GACOS, GLM, and BLM corrections. (a) and (b) are the GSTDs of the ascending and descending  
893 displacement time series, respectively, and (c) and (d) are the GSTD reduction percentages of the proposed  
894 method relative to the other two methods for the ascending and descending tracks, respectively

895  
896 **Fig. 17.** Displacement time series for the points PA1-PA2 and PD1-PD2 (marked in Fig. 15(a) and (d))  
897 calculated with the GACOS, GLM, and BLM corrections. (a) and (c) are points PA1 and PA2 from the  
898 ascending Sentinel-1 images, respectively; and (b) and (d) are points PD1 and PD2 from the descending  
899 Sentinel-1 images, respectively.